TOPOLOGICAL PHASES OF COLD ATOMS IN OPTICAL SUPERLATTICE

Fuyuki Matsuda

2020

Abstract

Recent remarkable development in experiments for cold atom systems enables us to simulate lattice systems which are hard to realize in solid-state systems. Thanks to the advantage of ultracold atomic systems, the high controllability of the parameters of the system and high resolution of the detection, numerous intriguing models have been realized in such cold atom systems. One of the examples for such realization is topological phases. Topological phases, of which geometric properties of wave functions are connected to transport phenomena, have been actively investigated both theoretically and experimentally in recent years. Motivated by these backgrounds, we study two kinds of topological phases which can be realized in ultracold atomic systems.

First, we analyze topological properties of the one-dimensional (1D) Bose-Hubbard model with a quasiperiodic superlattice potential. This system can be realized in interacting ultracold bosons in an optical lattice in the presence of an incommensurate superlattice potential. We first analyze the quasiperiodic superlattice made by the cosine function, which we call Harper-like Bose-Hubbard model. We compute the Chern number and observe a gap-closing behavior as the interaction strength U is changed. Also, we discuss the bulk-edge correspondence in our system. Furthermore, we explore the phase diagram as a function of U and a continuous deformation parameter β between the Harper-like model and another important quasiperiodic lattice, the Fibonacci model. We numerically confirm that the incommensurate charge density wave (ICDW) phase is topologically non-trivial and it is topologically equivalent in the whole ICDW region.

Second, we propose a two-dimensional (2D) version of Thouless pumping that can be realized by using ultracold atoms in optical lattices. To be specific, we consider a 2D square lattice tight-binding model with an obliquely introduced superlattice. It is demonstrated that quantized particle transport occurs in this system, and that the transport is expressed as a solution of a Diophantine equation. This topological nature can be understood by mapping the Hamiltonian to a three-dimensional (3D) cubic lattice model with a homogeneous magnetic field. We also propose a continuum model with obliquely introduced superlattice and obtain the amount of pumping by

calculating the Berry curvature. For this model, the same Diophantine equation can be derived from the plane-wave approximation. Furthermore, we investigate the effect of a harmonic trap by solving the time-dependent Schrödinger equation. Under a harmonic trap potential, as often used in cold atom experiments, we show, by numerical simulations, that nearly quantized pumping occurs when the phase of the superlattice potential is driven at a moderate speed. Also, we find that two regions appear, the Hofstadter region and the rectifying region, depending on the modulation amplitude of the superlattice potential. In the rectifying region with larger modulation amplitudes, we uncover that the pumping direction is restricted to exactly the x-axis or the y-axis direction. This difference in these two regions causes a crossover behavior, characterizing the effect of the harmonic trap.

This thesis is organized as follows. In Chapter 1 we give an overview of topological phases and ultracold atoms. In Chapter 2 we explain the numerical calculation methods which we used in this thesis. Topological aspects of the 1D Bose-Hubbard model with quasiperiodic modulation are discussed in Chapter 3. We propose new topological phases in a 2D optical superlattice model, and elucidate the topological nature of this model in Chapter 4. Chapter 5 concludes our results in this thesis.

Contents

List of publications

Papers related to the thesis

1. Fuyuki Matsuda, Masaki Tezuka, and Norio Kawakami
   Topological Properties of Ultracold Bosons in One-Dimensional Quasiperiodic Optical Lattice
   J. Phys. Soc. Jpn. **83**, 083707 (2014).

2. Fuyuki Matsuda, Masaki Tezuka, and Norio Kawakami
   Two-Dimensional Thouless Pumping of Ultracold Fermions in Obliquely Introduced Optical Superlattice
   J. Phys. Soc. Jpn. (in press)

Papers not included in the thesis

3. Fuyuki Matsuda, Masaki Tezuka, and Norio Kawakami
   Correlation Effects in One-Dimensional Quasiperiodic Anderson-Lattice Model
   Physics Procedia. **75**, 245 (2015).

Chapter 1 Introduction

The Nobel prize in 2016 has been awarded to David J. Thouless, F. Duncan M. Haldane, and John M. Kosterlitz for theoretical discoveries of topological phase transitions and topological phases of matter. In these phenomena, the physical quantities are described by topological invariants. Topological invariants, as typified by winding number, are robust against disorder and correlation. Returning to the Nobel prize, the reason of the award is based on three great theoretical discoveries:

1. Topological phase transition which occurs in thin layer (which is called Berezinskii-Kosterlitz-Thouless transition or Kosterlitz-Thouless transition today)

2. Integer quantum Hall effect and quantum pumping (which is called Thouless pumping)

3. Topological phase which can be realized in one-dimensional (1D) quantum spin models (this phase is called Haldane phase)

These results were the starting point of the research of topological phenomena which have been widely developed up to today. This thesis is deeply connected to the item 2: Integer quantum Hall effect and quantum pumping. In this thesis, we study two kinds of topological phases which can be realized in ultracold atomic systems. One is a 1D Bose-Hubbard model with quasiperiodic modulation, and the other is a two-dimensional (2D) square lattice model with obliquely introduced superlattice.

In section 1.1, an overview of the theory of the topological phases is given. In section 1.2, the properties of cold atom systems are described. The organization of this thesis is written in section 1.3.

1.1 Topological Phases

1.1.1 Berry phase

Berry phase is an important concept to understand topological physics. When the system is described by a parametrized Hamiltonian, a phase difference occurs after an adiabatic process whose parameter follows a cyclic path in the parameter space. This is called the Berry phase, or called the geometric phase, which is distinguished from the dynamic phase which occurs by dynamical process[1].

Consider a physical system which is described by a Hamiltonian parametrized by a set of parameters $\mathbf{R} = (R_1, R_2, \dots)$,

$$H = H(\mathbf{R}), \tag{1}$$

$$\mathbf{R} = \mathbf{R}(t). \tag{2}$$

Prepare the time-dependent Schrödinger equation,

$$H(\mathbf{R}(t)) \left|\psi(t)\right\rangle = i\hbar \frac{\partial}{\partial t} \left|\psi(t)\right\rangle, \tag{3}$$

and consider the case that the initial state is one of the eigenstates, and $\mathbf{R}$ moves slowly (adiabatically) and it comes back to the initial point after time T in $\mathbf{R}$ space ($\mathbf{R}(0) = \mathbf{R}(T)$). From the adiabatic theorem, if any two of $E_n(\mathbf{R})$ do not cross, the state at $t = T$ should come back to the initial state. However, there remains a freedom of phase, which can be expressed as $\psi(0) = e^{i\gamma(T)}\psi(T)$. Now we derive this phase $\gamma(T)$ below.

Let E_n and $|\phi_n(\mathbf{R})\rangle$ be a set of eigenvalues and eigenvectors of time-independent Schrödinger equation with Hamiltonian $H(\mathbf{R})$,

$$H(\mathbf{R}) \left|\phi_n(\mathbf{R})\right\rangle = E_n(\mathbf{R}) \left|\phi_n(\mathbf{R})\right\rangle. \tag{4}$$

Since we assume that $\mathbf{R}(t)$ is adiabatic, by applying the adiabatic theorem, we obtain

$$\left|\psi(t)\right\rangle = e^{i\gamma(t)} \left|\phi_n(\mathbf{R}(t))\right\rangle. \tag{5}$$

Here, $\gamma(t)$ is the phase factor.

From Eq. (3),

$$E_n\left(R(t)\right) = \langle\psi(t)|H(\mathbf{R}(t))|\psi(t)\rangle = i\hbar \left\langle\psi(t)\right| \frac{\partial}{\partial t} \left|\psi(t)\right\rangle. \tag{6}$$

On the other hand, by direct substitution of Eq. (4),

$$\langle\psi(t)|\frac{\partial}{\partial t}|\psi(t)\rangle = \langle\phi_n(\mathbf{R}(t))|e^{-i\gamma(t)}\frac{\partial}{\partial t}e^{i\gamma(t)}|\phi_n(\mathbf{R}(t))\rangle \tag{7}$$

$$= i\frac{\partial\gamma(t)}{\partial t} + \langle\phi_n(\mathbf{R})|\frac{\partial}{\partial\mathbf{R}}|\phi_n(\mathbf{R})\rangle \cdot \frac{\partial\mathbf{R}}{\partial t}. \tag{8}$$

By comparing Eq. (6) and Eq. (8),

$$i\frac{\partial}{\partial t}\gamma(t) = -\frac{i}{\hbar}E_n(\mathbf{R}(t)) - \langle\phi_n(\mathbf{R})|\frac{\partial}{\partial\mathbf{R}}|\phi_n(\mathbf{R})\rangle \cdot \frac{\partial\mathbf{R}}{\partial t}. \tag{9}$$

By integrating this, we obtain

$$\gamma(T) - \gamma(0) = -\frac{1}{\hbar}\int_0^\tau E_n(\mathbf{R}(t))dt + i\oint_C d\mathbf{R} \cdot \left\langle\phi_n(\mathbf{R})\right| \frac{\partial}{\partial\mathbf{R}} \left|\phi_n(\mathbf{R})\right\rangle. \tag{10}$$

The first term is a trivial term, which appears even when the Hamiltonian does not change, and this is called a dynamic phase. The second term only depends on geometric features of the integral contour C, but not depend on $R(t)$, which means how the contour is traversed (as long as the adiabatic condition is satisfied). This is why the Berry phase is also called the geometric phase.

The closed-path Berry phase can be written down as follows:

$$\gamma_n = i \oint_C d\mathbf{R} \cdot \mathbf{A}_n(\mathbf{R}), \tag{11}$$

$$\mathbf{A}_n(\mathbf{R}) = \langle \phi_n(\mathbf{R}) | \frac{\partial}{\partial \mathbf{R}} | \phi_n(\mathbf{R}) \rangle . \tag{12}$$

$\mathbf{A}_n(\mathbf{R})$ is called *Berry connection*. Berry connection is gauge-dependent, which transform as $\tilde{\mathbf{A}}_n(\mathbf{R}) = \mathbf{A}_n(\mathbf{R}) + \frac{\partial}{\partial \mathbf{R}} \lambda(\mathbf{R})$ under the gauge transformation $|\tilde{\phi}_n(\mathbf{R})\rangle = e^{-i\lambda(\mathbf{R})} |\phi_n(\mathbf{R})\rangle$. This is an analog of vector potential in electromagnetism. By considering this analogy, the closed-path Berry phase corresponds to the number of magnetic flux.

Berry curvature is an analog of the magnetic field in electromagnetism, and it is defined as an anti-symmetric second-rank tensor:

$$\Omega_{n,\mu\nu}(\mathbf{R}) = \frac{\partial}{\partial R^\mu} A_{n,\nu}(\mathbf{R}) - \frac{\partial}{\partial R^\nu} A_{n,\mu}(\mathbf{R}). \tag{13}$$

Here, $A_{n,\mu}(\mathbf{R})$ is a component of Berry connection $\mathbf{A}(\mathbf{R})$. Especially, when the dimension of parameter space is two ($\mathbf{R} = (R_1, R_2,)$), Berry curvature is expressed as

$$\Omega_n(\mathbf{R}) = \frac{\partial}{\partial R_1} A_{n,2}(\mathbf{R}) - \frac{\partial}{\partial R_2} A_{n,1}(\mathbf{R}). \tag{14}$$

By applying Stokes' theorem, the closed-path Berry phase can be rewritten as

$$\gamma_n = \int_S d\mathbf{S}\ \Omega_n(\mathbf{R}), \tag{15}$$

where S is an area surrounded by the closed path C. If the surface S is a closed manifold, this phase is restricted to integral multiple of 2π, and this integer is called *Chern number*:

$$C_n = \frac{i}{2\pi} \int_S d\mathbf{S} \left[\left\langle \frac{\partial \phi_n}{\partial R_1} \middle| \frac{\partial \phi_n}{\partial R_2} \right\rangle - \left\langle \frac{\partial \phi_n}{\partial R_2} \middle| \frac{\partial \phi_n}{\partial R_1} \right\rangle \right]. \tag{16}$$

This quantization of Chern number is guaranteed by Chern theorem (Chern-Gauss-Bonnet theorem). Finally, we note that the Berry curvature and the Chern number are gauge-invariant.

In the next section, we discuss Thouless pumping, which is an example where the Berry phase and the Chern number are related to the real physical phenomena.

1.1.2 Thouless pumping

In an infinite periodic system, if a potential varies slowly, the charge transfer over one period must have an integer value. Thouless found this fact in 1983 in his paper[2]. The reason of this quantization can be understood by expressing the charge transfer by the form of Chern number, which we have seen in the previous section.

Consider a time-dependent Schrödinger equation with time-dependent Hamlitonian,

$$i\hbar\frac{\partial}{\partial t}\Psi(x,t) = \hat{\mathrm{H}}(t)\Psi(x,t). \tag{17}$$

The eigenvalues $E_n(t)$ and eigenstates $\psi_n(x,t)$ for each moment of time-independent Schrödinger equation are also time-dependent,

$$\hat{H}(t)\psi(x,t) = E_n(t)\psi_n(x,t). \tag{18}$$

Here, we take a set of $\psi_n(x,t)$ which satisfies orthonormalization condition $\langle\psi_n(t)|\psi_m(t)\rangle = \delta_{nm}$.

Now, we express Ψ as a linear combination of ψ_n,

$$\Psi(t) = \sum_n c_n(t)\psi_n(t)e^{i\theta_n(t)}, \tag{19}$$

where

$$\theta_n(t) = -\frac{1}{\hbar}\int_0^t E_n(t')dt' \tag{20}$$

is called the dynamic phase factor. By putting Eq. (19) into Eq. (17), we obtain

$$i\hbar\sum_n(\dot{c}_n\psi_n + c_n\dot{\psi}_n + ic_n\psi_n\dot{\theta_n})e^{i\theta_n} = \sum_n c_n\hat{\mathrm{H}}\psi_n e^{i\theta_n}. \tag{21}$$

Since $\dot{\theta}_n = -\frac{E_n}{\hbar}$, the right hand and the third term of left hand cancel each other, and we obtain

$$\sum_n \dot{c}_n\psi_n e^{i\theta_n} = -\sum_n c_n\dot{\psi}_n e^{i\theta_n}. \tag{22}$$

That is,

$$\dot{c_m}(t) = -\sum_n c_n\langle\psi_m|\dot{\psi}_n\rangle e^{i(\theta_n-\theta_m)}. \tag{23}$$

In fact, $\psi_n(t)$ has a degree of freedom of selecting its phase. To remove this, we impose a conditon:

$$\langle\psi_0|\dot{\psi}_n\rangle = 0. \tag{24}$$

Then, $c_0(t)$ and $c_m(t)(m \neq 0)$ can be determined.

$$\dot{c_0}(t) = 0 \qquad \therefore c_0(t) = 1, \tag{25}$$

$$\dot{c_m}(t) = -\langle\psi_m|\dot{\psi}_0\rangle\, e^{i(\theta_0-\theta_m)} \tag{26}$$

$$= -\langle\psi_m|\dot{\psi}_0\rangle\, e^{-\frac{i}{\hbar}\int_0^t (E_0(t')-E_m(t'))dt'}, \tag{27}$$

$$c_m(t) = -\frac{\langle\psi_m|\dot{\psi}_0\rangle}{E_0-E_m} i\hbar e^{-\frac{i}{\hbar}\int_0^t (E_0(t')-E_m(t'))dt'}. \tag{28}$$

From Eqs. (19), (20), (25) and (28), we obtain $|\Psi(t)\rangle$ to the first order in the time derivatives:

$$|\Psi(t)\rangle \approx \exp\left[-(i/\hbar)\int^t \epsilon_0(t')\,dt'\right]\left[|\psi_0(t)\rangle + i\hbar\sum_{j\neq 0}|\psi_j(t)\rangle\,(\epsilon_j-\epsilon_0)^{-1}\left\langle\psi_j(t)\,\middle|\,\dot{\psi}_0(t)\right\rangle\right]. \tag{29}$$

By using a form of the particle current density $\mathbf{J} = \frac{\mathrm{d}}{\mathrm{d}t}(\psi^*\psi) = -\frac{\hbar}{2mi}\nabla\cdot\{\psi^*\nabla\psi - (\nabla\psi^*)\,\psi\}$, we obtain its expression to the same order,

$$\begin{aligned} J_0 &= \frac{\hbar^2}{mL}\sum_{j\neq 0}\frac{1}{(\epsilon_j-\epsilon_0)}\left[-\left\langle\psi_j\,\middle|\,\dot{\psi}_0\right\rangle\left\langle\frac{\partial\psi_0}{\partial x}\,\middle|\,\psi_j\right\rangle - \left\langle\dot{\psi}_0\,\middle|\,\psi_j\right\rangle\left\langle\psi_j\,\middle|\,\frac{\partial\psi_0}{\partial x}\right\rangle\right] \\ &= \frac{\hbar^2}{mL}\left[\left\langle\frac{\partial\psi_0}{\partial x}\,\middle|\,(\epsilon_0-H)^{-1}\,\middle|\,\dot{\psi}_0\right\rangle + \left\langle\dot{\psi}_0\,\middle|\,(\epsilon_0-H)^{-1}\,\middle|\,\frac{\partial\psi_0}{\partial x}\right\rangle\right]. \end{aligned} \tag{30}$$

For an infinite periodic system, Eq. (30) can be replaced by

$$J = \frac{\hbar^2}{2\pi m}\sum_{\lambda\mu}\int dk \frac{f_\lambda(1-f_\mu)}{\epsilon_\lambda(k)-\epsilon_\mu(k)}\left[\left\langle\frac{\partial\psi_{\lambda k}}{\partial x}\,\middle|\,\psi_{\mu k}\right\rangle\left\langle\psi_{\mu k}\,\middle|\,\dot{\psi}_{\lambda k}\right\rangle + \left\langle\dot{\psi}_{\lambda k}\,\middle|\,\psi_{\mu k}\right\rangle\left\langle\psi_{\mu k}\,\middle|\,\frac{\partial\psi_{\lambda k}}{\partial x}\right\rangle\right]. \tag{31}$$

By using this identity,

$$\frac{\partial\psi_{\lambda k}}{\partial k} = i[g(k)+x]\psi_{\lambda k} + \sum_{\mu\neq\lambda}\psi_{\mu k}\frac{1}{\epsilon_\lambda(k)-\epsilon_\mu(k)}\frac{i\hbar^2}{m}\left\langle\psi_{\mu k}\,\middle|\,\frac{\partial\psi_{\lambda k}}{\partial x}\right\rangle, \tag{32}$$

where $g(k)$ is an arbitrary real function, we can replace $[\epsilon_\lambda(k)-\epsilon_\mu(k)]^{-1}\,\partial/\partial x$ by $(im/\hbar^2)\,\partial/\partial k$. Integrating Eq. (31) by t for one cycle, the contribution of the first term in Eq. (32) vanishes. Then, we obtain the charge transfer in one cycle:

$$C = \frac{i}{2\pi}\sum_\lambda f_\lambda\int_0^T dt\int_0^{2\pi/L} dk\left[\left\langle\frac{\partial\psi_{\lambda k}}{\partial t}\,\middle|\,\frac{\partial\psi_{\lambda k}}{\partial k}\right\rangle - \left\langle\frac{\partial\psi_{\lambda k}}{\partial k}\,\middle|\,\frac{\partial\psi_{\lambda k}}{\partial t}\right\rangle\right]. \tag{33}$$

This can be regarded as the sum of Chern number Eq. (16) on the Brillouin zone, which is mathematically equal to torus.

Chern number is also related with the integer quantum Hall effect. In the next section, we discuss how the Chern number appears in a 2D electron system, where the integer quantum Hall effect appears.

1.1.3 Integer Quantum Hall Effect

One of the most surprising discoveries in 20th century is the discovery of the quantum Hall effect. von Klitzing *et al.* found that the Hall conductivity of the free electron system in a thin layer with strong magnetic field is quantized as follows[3]:

$$\sigma_{xy} = n\frac{e^2}{h} \quad (n : \text{integer}), \tag{34}$$

where e is the charge of electron and h is Planck constant. At first, the reason why the Hall conductivity is written by the multiple of e^2/h was unclear. However, the topological nature of this integer n has been revealed in the so-called "TKNN paper"[4]. Chern number is expressed as

$$N = \sum_m \frac{1}{2\pi i}\int dk_x dk_y \left(\left\langle \frac{\partial u_m}{\partial k_x} \middle| \frac{\partial u_m}{\partial k_y} \right\rangle - \left\langle \frac{\partial u_m}{\partial k_y} \middle| \frac{\partial u_m}{\partial k_x} \right\rangle \right), \tag{35}$$

where $|u_m(k)\rangle$ is m-th Bloch function.

Now we consider a 2D lattice system with a homogeneous magnet field.

$$H = \sum_{m,n} -t_a \hat{c}^\dagger_{m+1,n}\hat{c}_{m,n} - t_b \hat{c}^\dagger_{m,n+1}\hat{c}_{m,n}e^{i2\pi\Phi m} + \text{h.c.} \tag{36}$$

Next, we apply Fourier transform to the Hamiltonian, separate k_x into q blocks and let $k_x = k_x^0 + 2\pi\Phi n$. We obtain the Hamiltonian which is diagonal for k_x^0:

$$\begin{aligned}\hat{H}(k_x^0, k_y) = \sum_{n=0}^{q-1} \big\{ & -2t_a \cos\left(k_x^0 + 2\pi\Phi n\right) \hat{c}^\dagger \left(k_x^0 + 2\pi\Phi n, k_y\right) \hat{c}\left(k_x^0 + 2\pi\Phi n, k_y\right) \\ & -t_b \left(e^{-ik_y} \hat{c}^\dagger \left(k_x^0 + 2\pi\Phi(n+1), k_y\right) \hat{c}\left(k_x^0 + 2\pi\Phi n, k_y\right) \right. \\ & \left. + \; e^{ik_y} \hat{c}^\dagger \left(k_x^0 + 2\pi\Phi(n-1), k_y\right) \hat{c}\left(k_x^0 + 2\pi\Phi n, k_y\right) \right) \big\}.\end{aligned} \tag{37}$$

This Hamiltonian $\hat{H}_{k_x^0, k_y}$ can be interpreted as a q-cite 1D lattice. Using a set of coefficients $\{a_m\}$:

$$|\psi\rangle = \sum_{m=0}^{q-1} a_m \hat{c}^\dagger(k_x^0 + 2\pi\Phi m, k_y)|0\rangle, \tag{38}$$

the eigenvalue equation is

$$-2t_a \cos\left(k_x^0 + 2\pi\Phi n\right) a_n - t_b \left(e^{-ik_y} a_{n-1} + e^{ik_y} a_{n+1}\right) = E_{k_x^0, k_y} a_n. \tag{39}$$

This is called Harper equation, and the boundary condition is $a_{j+q} = a_j$. By solving Harper equation, we can obtain eigenenergies of this system. When we plot eigenenergies in different strengths of the magnetic field, a butterfly structure in Figure 1.1 appears[5].

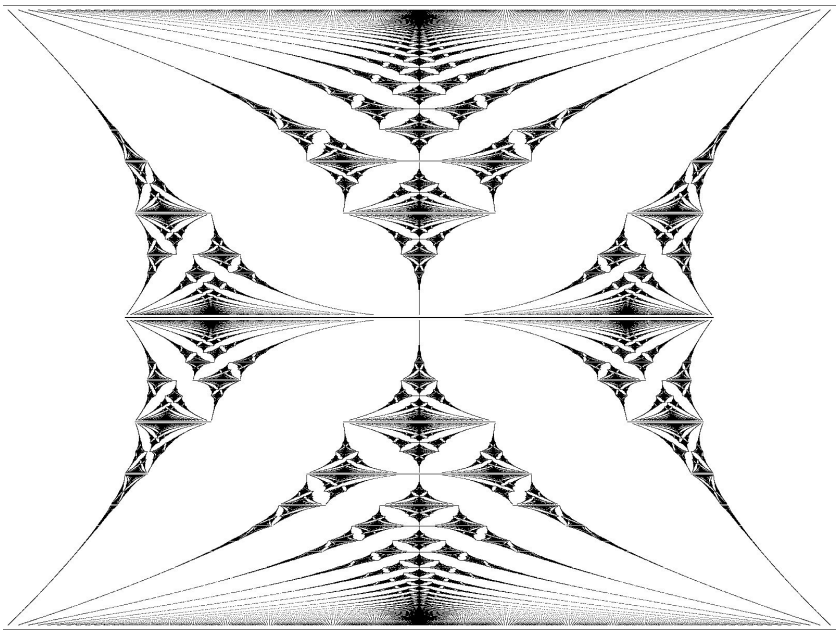

Figure 1.1: Hofstadter Butterfly. The vertical line shows the strength of the magnetic field, and the horizontal line shows an energy spectrum of the Hamiltonian for each magnetic field strength.

Eq. (39) is derived from the 2D square lattice with the magnet field. However, Eq. (39) can also be interpreted as an eigenvalue equation of a 1D lattice with a cosine type potential. This implies that the 2D system with the magnet field and the 1D lattice with superlattice are equivalent in the topological context. This correspondence also appears in the definition of topological invariants. As we have seen in the previous section, the pumped charge for one cycle is written as:

$$C = \frac{i}{2\pi} \sum_{\lambda} f_{\lambda} \int_0^T dt \int_0^{2\pi/L} dk \left[\left\langle \frac{\partial \psi_{\lambda k}}{\partial t} \middle| \frac{\partial \psi_{\lambda k}}{\partial k} \right\rangle - \left\langle \frac{\partial \psi_{\lambda k}}{\partial k} \middle| \frac{\partial \psi_{\lambda k}}{\partial t} \right\rangle \right]. \tag{40}$$

This has the same form with Eq. (35). Now, if we match the notation of Hamiltonians of 1D quantum pumping and 2D quantum Hall system, each Hamiltonian can be written as:

$$\mathcal{H}(\phi) = \sum_j \left[-t \left(\hat{c}_{j+1}^{\dagger} \hat{c}_j + \hat{c}_{j-1}^{\dagger} \hat{c}_j \right) + \lambda \cos(2\pi b j + \phi) \hat{c}_j^{\dagger} \hat{c}_j \right], \tag{41}$$

$$\mathcal{H} = \sum_{m,n} \left[-t \left(c_{m,n+1}^{\dagger} c_{m,n} + c_{m,n-1}^{\dagger} c_{m,n} \right) + \frac{\lambda}{2} \left(e^{i2\pi bn} c_{m+1,n}^{\dagger} c_{m,n} + e^{-i2\pi bn} c_{m-1,n}^{\dagger} c_{m,n} \right) \right]. \tag{42}$$

These two Hamiltonians can be mapped to each other by Fourier transform and inverse Fourier transform. We note that a parameter, a phase of the twisted boundary condition θ, is hidden in Eq. (41). To calculate the energy spectrum of Eq. (41), we need to set θ. Finally, we summarize the correspondence between 1D quantum pumping and 2D quantum Hall system in Table 1.1.

	1D quantum pumping	2D quantum Hall system
b	Periodicity of superlattice	Magnetic field strength
ϕ	Phase of superlattice	Wavenumber k_y
θ	Phase of twisted boundary condition	Wavenumber k_x
C	Charge pumping amount	Hall conductivity

Table 1.1: The correspondence between 1D quantum pumping and 2D quantum Hall system.

1.2 Ultracold Atoms

Ultracold atoms are drawing attention as a platform of quantum simulator. Quantum simulator enables us to study systems which are hard to control in the laboratory by transforming them into a controllable, accessible system. R. P. Feynman gave a lecture about physics and computation at MIT in 1981[6], and left an impressive phrase:

> "Nature isn't classical, dammit, and if you want to make a simulation of nature, you'd better make it quantum mechanical, and by golly it's a wonderful problem, because it doesn't look so easy."

He pointed out that classical computer (probabilistic simulator) cannot represent the result of quantum mechanics, because of a consequence of hidden-variable problem. Of course, it is possible to track a density matrix of the whole quantum system and simulate them. However, when the system has many particles, the degree of freedom explodes exponentially, and we need exponentially large computer to simulate it. This is why we need a quantum simulator to simulate quantum systems. Recently, thanks to a remarkable development of ultracold atom experiment, ultracold atomic system becomes one of great platforms of quantum simulator.

Ultracold atoms are atoms that are trapped in vacuum by using a magnetic or optical field, and maintained at temperatures usually below microkelvin (μK) order. At this temperature, the quantum effect becomes principal and quantum condensation occurs to the mass of atoms. To realize this very low temperature, the experimental

technique, which is called laser cooling and evaporative cooling, is used. Ultracold atoms are often used to simulate a quantum system since it is very clean system and has very little noise or disturbance. The system of ultracold atoms has many suitable properties to simulate quantum systems. We close up three properties of ultracold atoms, 1. High controllability of physical parameters, 2. Richness of detection methods, 3. Exotic phases realization by using synthetic gauge fields.

One of the most characteristic properties of ultracold atomic systems is the high controllability of the physical parameters. *Feshbach resonance* enables us to control the interaction strength between atoms. The low energy physics of scattering is characterized by a parameter called scattering length. Usually, scattering length only depends on interatomic potential. However, when the energy of the bound state (molecular state) and the kinetic energy of the scattering state become close, a resonance which is called Feshbach resonance occurs. In order to adjust the energy level of different spin states, a magnetic field can be used in the experiments of ultracold atoms. A magnetically tuned Feshbach resonance is described in a simple expression. According to Ref. [7, 8], the s-wave scattering length a as a function of the magnetic field B is expressed as:

$$a(B) = a_{\mathrm{bg}} \left(1 - \frac{\Delta}{B - B_0} \right), \tag{43}$$

where a_{bg} is the background scattering length, B_0 is the resonance position, and Δ is the resonance width. This technique enables us to access a new parameter region which cannot be reached in other systems, such as BEC-BCS crossover. Also, it is possible to simulate the important models in physics, for example, Hubbard model, Kondo lattice model, and so on. Feshbach resonance makes it possible to control the interaction strength in these lattice models, while a controlling parameter is very hard in solid systems.

To construct a lattice of ultracold atomic system, an *optical lattice* is used. The optical lattice is formed by counter-propagating laser beams, which make a standing wave. When atoms are placed in this oscillating optical field, a dipole moment occurs in the atom, and it interacts with the electric field and causes an energy shift. This is called AC stark shift, which is expressed as

$$V(\mathbf{r}) = -\frac{1}{2}\alpha(\omega)|\mathbf{E}(\mathbf{r})|^2, \tag{44}$$

where $\alpha(\omega)$ is the AC polarizability and $|\mathbf{E}(\mathbf{r})|^2$ is the strength of AC electric field which is averaged by time. For example, in a 1D system, we can prepare a lattice by using the standing wave $|\mathbf{E}(\mathbf{r})|^2 = E^2 \cos^2(\mathbf{k} \cdot \mathbf{r})$. When the lattice depth is sufficiently deep, it is useful to express a Hamiltonian in Wannier functions. Then

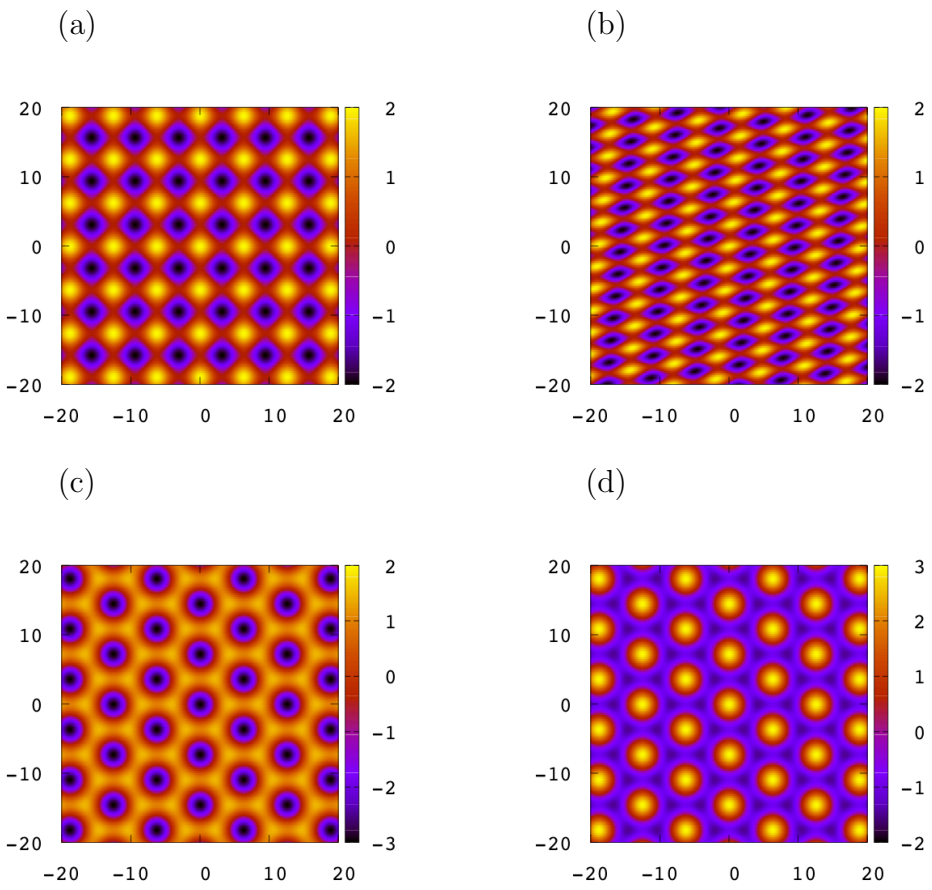

Figure 1.2: Various optical lattices. (a) Square lattice, (b) Parallelogram lattice, (c) Triangular lattice, (d) Hexiagonal lattice. See also [9, 10]

the Hamiltonian of ultracold atoms in optical lattice can be described by a Hubbard model, which is written as:

$$H_{BH} = -t \sum_{\langle i,j \rangle} \left(b_i^\dagger b_j + \text{h.c.} \right) + \frac{U}{2} \sum_j n_j \left(n_j + 1 \right) \tag{45}$$

for bosons and

$$H_{FH} = -t \sum_{\langle i,j \rangle, \sigma} \left(c_{i\sigma}^\dagger c_{j\sigma} + \text{h.c.} \right) + U \sum_j n_{j\uparrow} n_{j\downarrow} \tag{46}$$

for fermions. Feshbach resonance allows one to tune the on-site interaction strength. By using this technique, many kinds of exotic phases have been realized, for instance, bosonic Mott insulator [11, 12, 13], fermionic Mott insulator [14, 15], SU(N) [16, 17].

Second surprising point of cold atom systems is various probing methods. *Time-of-flight (ToF)* method has been a good method to measure temperature and momentum distribution [18, 19, 20]. After cooling the atoms, by switching off the magnetic or optical trap, atoms get free from trap potential. After that, atoms move by initial speed distribution and start to drop freely by gravity. When sufficient time has been passed, the space distribution of atom cluster is reflected by initial speed distribution. By taking a photograph of this atom cluster, it is possible to obtain speed distribution (or momentum distribution). *Quantum gas microscope* enables observation and control of quantum system in the level of individual atoms. It is possible to take a snapshot of real space distribution. Moreover, single-site spin control is realized, and arbitrary spin patterns can be prepared. These techniques are important to compose a quantum simulator. Also, these detection methods enable us to investigate the dynamics or thermalization of quantum systems. [21]

The last important possibility of ultracold atoms which we see in this section is *artificial gauge fields*. Since the atoms are electrically neutral, atoms never experience electric field and Lorentz forces. The first realization of artificial gauge field is using Coriolis force in the rotating frame [22, 23, 24]. However, this method can only make a weak gauge field. To overcome this problem, a new method to make a strong gauge field has been investigated, which is called laser-induced gauge field. This method uses an internal degree of freedom to construct a Berry phase. For example, let us consider a two-level atom which has the ground state $|g\rangle$ and an excited state $|e\rangle$. When the laser beam is distributed to the system, two levels are coupled by this beam. If the laser intensity and phase are varying spatially, a proportion of coupling also varies. This causes a Berry phase, which would be a substitution of an Aharonov-Bohm phase.

Some of the important models of topological phases are succeeded to capture the essence of the requirement for making topological phases. However, it is hard to realize

in conventional materials. Recently, several groups realized various lattice models for topological phases. For instance, 1D topological phases such as Topological pumping [25, 26], Rice-Mele model/Su-Schrieffer-Heeger (SSH) model [27], Harper model[28, 29] are realized. In 2D, Hofstadter model, Haldane model [28] are actualized. Also, many exotic setups are theoretically proposed. For example, three-dimensional (3D) Dirac fermions [30, 31], Weyl semimetals [32], 3D Z_2 topological insulators [33], Hopf insulators [34] are proposed. Moreover, by using initial degree of freedom of the atoms, one can construct synthetic dimensions [35, 36, 37]. By using this idea, it is possible to realize not only 2D topological phase, but also four-dimensional (4D) quantum Hall system, which is described by second Chern number [38].

1.3 Organization of the thesis

As summarized above, cold atom systems experiments are extremely developed recently. This enables us to simulate lattice systems, which are hard to realize in solid-state systems. Also, topological phases have been actively investigated both theoretically and experimentally in recent years. Motivated by these backgrounds, we study two kinds of topological phases, 1D Bose-Hubbard model with quasiperiodic modulation and 2D optical superlattice model, which can be realized in ultracold atom systems.

This thesis is organized as follows. In Chapter 2, we explain the numerical calculation methods, exact diagonalization (Lanczos method), density matrix renormalization group, Fukui–Hatsugai–Suzuki method, and time-dependent Schrödinger equation, which we used in this thesis. In Chapter 3, we discuss the topological nature of a 1D Bose-Hubbard model with quasiperiodic modulation. Furthermore, we investigate the phase diagram as a function of the interaction strength U and the potential deformation parameter β. New topological phases in the 2D optical superlattice model are proposed, and the topological nature of this model is elucidated in Chapter 4. We investigate three models, tight-binding model, continuum model, and continuum model with a harmonic trap and show that the amount of pumping is provided by the Diophantine equation. Also, we studied the effects of the harmonic trap. We conclude our results in this thesis in Chapter 5.

Chapter 2 Numerical Calculation Methods

When we treat the problem of condensed matter physics such as many body systems with interaction, it is possible to calculate rigorously when the system is small, but the calculation time explodes exponentially as the system size becomes bigger. In this dissertation, we use exact diagonalization for one body problem or small system size, and we use density matrix renormalization group (DMRG) for a problem which has a large system size. DMRG is a very powerful method to treat 1D systems.

In addition, some problems occur when we discretize continuous systems in order to calculate integral or differential equation. For example, to calculate a Chern number by discretizing the Brillouin zone straightforwardly, very dense mesh is needed. This problem can be resolved by using a method called Fukui-Hatsugai-Suzuki method. Also, there exists a numerically stable method, which can reduce the calculation time, to solve a time-dependent Schrödinger equation.

In this chapter, we outline how to use these four methods, exact diagonalization, DMRG, Fukui-Hatsugai-Suzuki method, and a method which we used to solve a time-dependent Schrödinger equation. In Sec. 2.1, we explain exact diagonalization method. In Sec. 2.2, DMRG method is described. In Sec. 2.3, Fukui-Hatsugai-Suzuki method is explained. Finally, we introduce a method which we used to solve a time-dependent Schrödinger equation in Sec. 2.4.

2.1 Exact Diagonalizaton (Lanczos Method)

Exact Diagonalization is a numerical computation method which calculates the eigenenergies and the eigenstates by writing up all of the basis sets of the system and diagonalizing the Hamiltonian matrix. When the dimension of Hamiltonian is up to $\sim 10^4$, there are appropriate methods such as Jacobi method or Householder method. However, when the dimension is larger, up to about $\sim 10^8$, and when the Hamiltonian matrix is sparse, Lanczos method is effective[39]. Lanczos method can only obtain the smallest m eigenvalues and corresponding eigenvectors. Nevertheless, in most cases of condensed matter physics, low-energy levels are important. Also, Hamiltonian in most of the models are sparse matrix. Therefore, Lanczos method is one of the best ways to calculate eigenvalues and eigenvectors numerically.

Here, we introduce Lanczos method. Suppose that an n-dimensional symmetric

matrix A is transformed into a tridiagonal matrix B by using a unitary matrix P, we obtain the following relation.

$$B = P^{-1}AP \iff PB = AP. \tag{47}$$

Since B is a tridiagonal matrix, B can be written as

$$B = \begin{pmatrix} \alpha_1 & \beta_1 & 0 & & & \\ \beta_1 & \alpha_2 & \beta_2 & 0 & & \\ 0 & \beta_2 & \alpha_3 & \beta_3 & \ddots & \\ & 0 & \beta_3 & \ddots & \ddots & 0 \\ & & \ddots & \ddots & & \beta_{n-1} \\ & & & 0 & \beta_{n-1} & \alpha_n \end{pmatrix}. \tag{48}$$

Let $P = (\boldsymbol{u}_1\boldsymbol{u}_2 \ldots \boldsymbol{u}_n)$. Then according to Eq. (47), we obtain

$$\begin{cases} A\boldsymbol{u}_1 = \alpha_1\boldsymbol{u}_1 + \beta_1\boldsymbol{u}_2, \\ A\boldsymbol{u}_2 = \beta_1\boldsymbol{u}_1 + \alpha_2\boldsymbol{u}_2 + \beta_2\boldsymbol{u}_3, \\ A\boldsymbol{u}_3 = \beta_2\boldsymbol{u}_2 + \alpha_3\boldsymbol{u}_3 + \beta_3\boldsymbol{u}_4, \\ \quad \vdots \\ A\boldsymbol{u}_n = \beta_{n-1}\boldsymbol{u}_{n-1} + \alpha_n\boldsymbol{u}_n. \end{cases} \tag{49}$$

With a condition that $\boldsymbol{u}_i$ is orthonormal, we derive

$$\begin{aligned} \alpha_i &= \boldsymbol{u}_i^\dagger A\boldsymbol{u}_i, \\ \beta_i &= \sqrt{(A\boldsymbol{u}_i - \beta_{i-1}\boldsymbol{u}_{i-1} - \alpha_i\boldsymbol{u}_i)^\dagger(A\boldsymbol{u}_i - \beta_{i-1}\boldsymbol{u}_{i-1} - \alpha_i\boldsymbol{u}_i)}, \\ \boldsymbol{u}_{i+1} &= \frac{A\boldsymbol{u}_i - \beta_{i-1}\boldsymbol{u}_{i-1} - \alpha_i\boldsymbol{u}_i}{\beta_i}. \end{aligned} \tag{50}$$

Consequently, if we prepare an n-dimensional vector $\boldsymbol{u}_1$, we can obtain $\alpha_1, \beta_1, \boldsymbol{u}_2, \alpha_2, \beta_2, \boldsymbol{u}_3, \ldots$, one after another. Usually, we use random numbers to determine the trial vector $\boldsymbol{u}_1$. These $\{\alpha_i\}$ and $\{\beta_i\}$ are the matrix elements of the tridiagonal matrix which we need. Finally, we diagonalize the tridiagonal matrix B. This can be done by $\mathcal{O}(N)$ calculation.

The characteristic point of Lanczos method is that we can cut off the procedure to obtain the matrix elements of the tridiagonal matrix. Calculating eigenvalues and eigenvectors of the cut-offed tridiagonal matrix gives an approximation of counterparts of the original matrix. This is very important to accelerate the calculation. This can be understood as follows.

Let $\lambda_1, \lambda_2, \ldots$ be the eigenvalues and let $\boldsymbol{x}_1, \boldsymbol{x}_2 \ldots$ be the corresponding eigenvectors in descending order of the absolute value. If a trial vector $\boldsymbol{u}_1$ is not orthogonal to $\boldsymbol{x}_1, \boldsymbol{x}_2 \ldots$, $\boldsymbol{u}_1$ can be written as:

$$\boldsymbol{u}_1 = c_1\boldsymbol{x}_1 + c_2\boldsymbol{x}_2 + \cdots \quad (c_1, c_2, \cdots \neq 0)\,. \tag{51}$$

In the procedures of Lanczos method, as in Eq. (50), we make $\boldsymbol{u}_{i+1}$ by multiplying $\boldsymbol{u}_i$ by A and subtract the component parallel to $\boldsymbol{u}_i$. While we construct $\boldsymbol{u}_m$, $\boldsymbol{u}_1$ has been multiplied $m-1$ times by A. $A^{m-1}\boldsymbol{u}_1$ can be written in terms of eigenvectors $\{\boldsymbol{x}_i\}$:

$$A^{m-1}\boldsymbol{u}_1 = c_1\lambda_1^{m-1}\boldsymbol{x}_1 + c_2\lambda_2^{m-1}\boldsymbol{x}_2 + \cdots \tag{52}$$

Therefore, we expect that a characteristic space which is based upon $\boldsymbol{u}_1, \boldsymbol{u}_2, \ldots \boldsymbol{u}_m$ contains $\boldsymbol{x}_1, \boldsymbol{x}_2, \ldots$ sufficiently. At this time, the larger the eigenvalue, the faster the eigenvector $\boldsymbol{x}_1$ appears in a characteristic space based upon $\boldsymbol{u}_1, \boldsymbol{u}_2, \ldots \boldsymbol{u}_m$. Accordingly, we should add (or subtract) a multiple of a unit matrix in order to maximize the absolute value of the eigenvalue which we need.

Method

1. Determine trial vector $\boldsymbol{u}_1$.

2. Calculate $\boldsymbol{v} = A\boldsymbol{u}_k$,
$$v_i = \sum_{j=1}^{n} a_{ij}u_j^{(k)}. \tag{53}$$

3. Calculate α_k, β_k, and the vector $\boldsymbol{u}_{k+1}$,
$$\begin{aligned} \alpha_k &= \sum_{i=1}^{n} v_i^* u_i^{(k)}, \\ \beta_k &= \sqrt{\sum_{i=1}^{n} |v_j - \beta_{k-1}u_i^{(k-1)} - \alpha_k u_i^{(k)}|^2}, \\ u_i^{(k+1)} &= \frac{v_i - \beta_{k-1}u_i^{(k-1)} - \alpha_k u_i^{(k)}}{\beta_k}. \end{aligned} \tag{54}$$

4. Redefine $\boldsymbol{u}_{k+1}$ by using Gram-Schmidt orthonormalization so that it is strictly orthogonal with $\boldsymbol{u}_1$, $\boldsymbol{u}_2$, $\ldots \boldsymbol{u}_{k-2}$ (this step is needed to keep numerical accuracy),
$$\boldsymbol{u}_{k+1} := \boldsymbol{u}_{k+1} - \sum_{i=1}^{k-2} \frac{\boldsymbol{u}_i^\dagger \boldsymbol{u}_{k+1}}{\boldsymbol{u}_i^\dagger \boldsymbol{u}_i}\boldsymbol{u}_i. \tag{55}$$

5. Repeat 1) to 4). Let the repetition number m.

6. Calculate eigenvalues λ_k and eigenvectors $\tilde{\boldsymbol{x}}_k$ of $m \times m$ dimensional tridiagonal matrix B, and obtain eigenvectors $\boldsymbol{x}_k$ of the original matrix A by using

$$\boldsymbol{x}_k = \sum_{i=1}^{m} \tilde{x}_i^{(k)} \boldsymbol{v}_i. \tag{56}$$

2.2 DMRG

Density matrix renormalization group (DMRG) is a numerical method for calculating low-energy physics of quantum many-particle systems. In many-particle systems, when a system size is large, the dimension of Hilbert space becomes exponentially large. This makes it very difficult to calculate physical quantities numerically. To avoid this difficulty, a method called numerical renormalization group (NRG) has been proposed. This method enables to calculate exponentially large Hilbert space by starting the calculation from a small system, and enlarge the system a little, and cutoff the eigenvalues/eigenvectors except we choose beforehand, and repeat this loop until we reach the system size that we aim at. By using this method, it should be possible to treat arbitrary system sizes. However, while NRG succeeded for the Kondo model, it is not successful in the Hubbard model and the Heisenberg model. This is because an edge effect remains while enlarging the system size.

In 1992, Steve White introduced DMRG method. In DMRG, the environment is added to the system, which enables us to take quantum fluctuations into account, a fluctuation which is spread through outside of the system in practice. Because of this treatment, DMRG succeeded in canceling the edge effect[40, 41]. DMRG allows to investigate the properties of spin chain systems such as the Ising model, the Heisenberg model, and also fermion/boson systems such as the Hubbard model. Especially, very accurate results have been obtained in 1D systems. DMRG is also precise in tree structure systems or 2D rectangular systems where one side is much longer than the other side. Recently, a matrix product state, which is a basic idea of DMRG, is applied to 2D and 3D systems [42, 43].

Basic idea

In DMRG, we separate the whole system into a system and an environment, and we call them a superblock altogether. While enlarging the system, we choose eigenvalues/eigenvectors which we should keep. To choose them, we take a partial trace for environment and leave the eigenvectors which have larger eigenvalues of its density matrix. Because of this approach, it is possible to take the effects of the outside of the

system, where NRG could not take into account, and possible to leave the important degrees of freedom.

Now, we introduce a basic idea of DMRG. First, write down the ground state as follows:

$$|\psi\rangle = \sum_{i,j} \psi_{ij} |i\rangle |j\rangle . \tag{57}$$

Here, $|i\rangle$ is the basis of the system (l dimensions), $|j\rangle$ is the basis of the environment. To reduce the calculation time, we need to decrease the dimensions of Hilbert space. Now, we reduce the dimension of eigenstates to m. Let this basis be $|u^\alpha\rangle$. Similarly, we reduce the dimension of environment to m, and let its basis be $|v^\alpha\rangle$. By using these bases, we can write an approximation of $|\psi\rangle$ as

$$|\bar{\psi}\rangle = \sum_{i,j} \sum_{\alpha=1}^{m} c_\alpha u_i^\alpha v_j^\alpha |i\rangle |j\rangle . \tag{58}$$

Using the singular value decomposition of ψ_{ij} (Here, U, V are unitary matrices),

$$\psi_{ij} = \sum_k U_{ik} d_k V_{jk}, \tag{59}$$

the norm of the difference between the original wave function and the approximated wave function can be written as

$$S = \| |\psi\rangle - |\bar{\psi}\rangle \|^2 = \sum_{i,j} \left(\sum_k U_{ik} d_k V_{jk} - \sum_{\alpha=1}^{m} c_\alpha u_i^\alpha v_j^\alpha \right)^2 . \tag{60}$$

Therefore, in order to minimize S, we should choose the largest m singular values d_k and use them as c_α, and bring u and v from corresponding U and V.

Between singular values d_k and the eigenvalues ω_k of the reduced density matrix of the system ρ, there is a relationship $\omega_k = d_k^2$. This is the reason why we take the largest m singular values d_k instead of eigenvalues ω_k. Then, the sum of cut-offed eigenvalues is an estimation of an error. Therefore, a difference between 1 and

$$P_m = \sum_{\alpha=1}^{m} \omega_\alpha \tag{61}$$

would be the estimation of an error (*cf.* Sum of density matrix is always 1).

Infinite size DMRG

We explain the 1D boson lattice model as an example. The superblocks which we consider in a process of the calculation is made by four blocks as we showed in 2.1.

Now we label them i_1, i_2, i_3, i_4 from the left to right side. i_1 and i_4 consist of an l-site system, and i_2 and i_3 consist of a 1-site system. Let $\mathcal{H}_1$, $\mathcal{H}_2$, $\mathcal{H}_3$, $\mathcal{H}_4$ be Hamiltonians in each block. Also, let $\mathcal{H}_{12}$, $\mathcal{H}_{23}$, $\mathcal{H}_{34}$ be Hamlitonians which extends over two blocks. Especially, when the system consists of an n-site system, we write down the Hamiltonians for i_1 and i_4 as $H^{\mathrm{L}}_{\mathrm{B}_n}$, $H^{\mathrm{R}}_{\mathrm{B}_n}$ respectively.

1. We start the calculation from the $n = 1$ case. Calculate matrix elements of each block Hamiltonian ($\langle i_1|\mathcal{H}_1|i'_1\rangle$, $\langle i_2|\mathcal{H}_2|i'_2\rangle$, $\dots$) and matrix elements of the two-block Hamiltonian such as $\mathcal{H}_{12}$ ($\langle i_1 i_2|\mathcal{H}_{12}|i'_1 i'_2\rangle$, $\dots$).

2. Make a matrix representation of the superblock Hamlitonian $\mathcal{H}_{1234}$ from the matrix elements which are calculated in 1).

$$\begin{aligned}
&\langle i_1 i_2 i_3 i_4|\mathcal{H}_{1234}|i'_1 i'_2 i'_3 i'_4\rangle \\
&\quad = \langle i_1|\mathcal{H}_1|i'_1\rangle \langle i_2 i_3 i_4|i'_2 i'_3 i'_4\rangle + \langle i_2|\mathcal{H}_2|i'_2\rangle \langle i_1 i_3 i_4|i'_1 i'_3 i'_4\rangle \\
&\qquad + \langle i_3|\mathcal{H}_3|i'_3\rangle \langle i_1 i_2 i_4|i'_1 i'_2 i'_4\rangle + \langle i_4|\mathcal{H}_4|i'_4\rangle \langle i_1 i_2 i_3|i'_1 i'_2 i'_3\rangle \\
&\qquad + \langle i_1 i_2|\mathcal{H}_{12}|i'_1 i'_2\rangle \langle i_3 i_4|i'_3 i'_4\rangle + \langle i_2 i_3|\mathcal{H}_{23}|i'_2 i'_3\rangle \langle i_1 i_4|i'_1 i'_4\rangle + \langle i_3 i_4|\mathcal{H}_{34}|i'_3 i'_4\rangle \langle i_1 i_2|i'_1 i'_2\rangle
\end{aligned} \tag{62}$$

3. Diagonalize the superblock Hamiltonian $\mathcal{H}_{1234}$ by using Lanczos method and obtain the ground state $|\psi\rangle$.

$$|\psi\rangle = \sum_{i_1 i_2 i_3 i_4} \psi_{i_1 i_2 i_3 i_4} |i_1 i_2 i_3 i_4\rangle \tag{63}$$

4. Trace out the environment blocks from the ground state in 3) and obtain a density matrix of system blocks.

$$\langle i_1 i_2|\rho|i'_1 i'_2\rangle = \sum_{i_3 i_4} \psi_{i_1 i_2 i_3 i_4} \psi_{i'_1 i'_2 i_3 i_4} \tag{64}$$

5. Diagonalize the density matrix $\rho_{i_1 i_2 i'_1 i'_2}$ and obtain m eigenvalues ω_α from the largest ones and their eigenvectors.

$$|u^\alpha\rangle = \sum_{i_1 i_2} u^\alpha_{i_1 i_2} |i_1 i_2\rangle \qquad (\alpha = 1, 2, \dots, m) \tag{65}$$

   Note that we obtain all of the eigenvalues and eigenvectors of the density matrix when the system size is small and the dimension of the density matrix $\rho_{i_1 i_2 i'_1 i'_2}$ is smaller than m at the beginning of the calculation.

6. Calculate the matrix elements of operators in the system (*i.e.*, creation/annihilation operator) for example, $\langle i_1 i_2|b^\dagger_j|i'_1 i'_2\rangle$, $\langle i_1 i_2|b_j|i'_1 i'_2\rangle$.

7. Apply a basis transformation to the operator which we made in 6) by using eigenvectors $u^{\alpha}_{i_1 i_2}$ of density matrix $\rho_{i_1 i_2 i'_1 i'_2}$.

$$\langle u^{\alpha}|\mathcal{H}^{L}_{B_{n+1}}|u'^{\alpha}\rangle = \sum_{i_1 i_2 i'_1 i'_2} \langle u^{\alpha}|i_1 i_2\rangle \langle i_1 i_2|(\mathcal{H}_1 + \mathcal{H}_2 + \mathcal{H}_{12})|i'_1 i'_2\rangle \langle i'_1 i'_2|u'^{\alpha}\rangle \quad (66)$$

Here, $\langle i_1 i_2|u'^{\alpha}\rangle = u^{\alpha}_{i_1 i_2} \quad (\alpha = 1, 2, \ldots, m)$.

8. Let $\mathcal{H}^{\mathrm{L}}_{\mathrm{B}_{n+1}}$ be a new block 1 and let $\mathcal{H}^{\mathrm{R}}_{\mathrm{B}_{n+1}}$ be a new block 4. Add two sites between them and let them a new block 2 and block 3. Construct a new superblock by these block 1∼4.

9. Go back to 2) and repeat the iteration until the system size reaches the goal size.

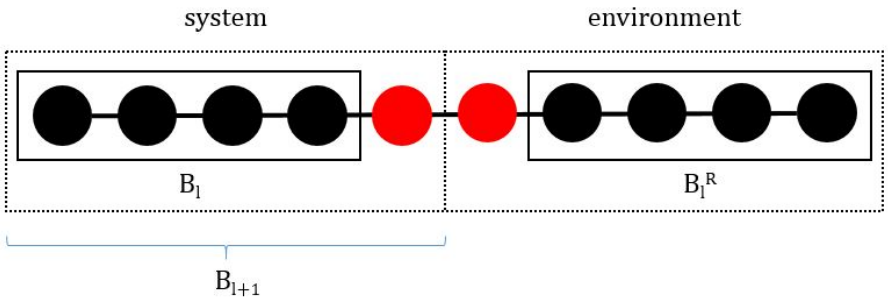

Figure 2.1: A schematic diagram of the superblock of infinite-size DMRG.

Finite size DMRG

Now we consider a finite size system which has N sites. In order to improve the accuracy of the calculation in the finite size system, we perform a procedure called "sweep". In infinite size DMRG, we only used B_n to construct B_{n+1}, but in finite size DMRG, we need $N-3$ type of blocks $B_1 \cdots B_{N-3}$. The procedure is as follows. Here, we explain it when N is an even number. When N is an odd number, we should take B^L for 1 site and B^R for 0 site, and the remaining procedures are the same.

1. Construct $B^L_2 \cdots B^L_{N/2}$ and $B^R_2 \cdots B^R_{N/2}$ by using infinite DMRG method. In this case, we need to keep the operator $c, c^{\dagger}$ of an edge of the block.

$$\begin{aligned} B^L_1 \bullet\bullet B^R_1 &\to B^L_2, B^R_2 \\ B^L_2 \bullet\bullet B^R_2 &\to B^L_3, B^R_3 \\ &\vdots \\ B^L_{N/2-1} \bullet\bullet B^R_{N/2-1} &\to B^L_{N/2}, B^R_{N/2} \end{aligned} \quad (67)$$

2. Let n be the size of B^L. First, we start from $n = N/2$. Fix the size of the superblock, and shift the position of the two sites between B^L and B^R (DMRG sweep). Construct $B^L_{N/2+1}, B^L_{N/2+2}, \cdots, B^L_{N-3}$ by this procedure.

$$\begin{aligned} B^L_{N/2} \bullet\bullet B^R_{N/2-2} &\to B^L_{N/2+1}, B^R_{N/2-3} \\ B^L_{N/2+1} \bullet\bullet B^R_{N/2-3} &\to B^L_{N/2+2}, B^R_{N/2-4} \\ &\vdots \\ B^L_{N-4} \bullet\bullet B^R_2 &\to B^L_{N-3}, B^R_1 \end{aligned} \tag{68}$$

3. Next, we start from $n = N - 3$ and sweep to left. Renew $B^R_2, B^R_3, \cdots, B^R_{N-3}$ by this procedure.

$$\begin{aligned} B^L_{N-3} \bullet\bullet B^R_1 &\to B^R_2 \\ B^L_{N-4} \bullet\bullet B^R_2 &\to B^R_3 \\ &\vdots \\ B^L_2 \bullet\bullet B^R_{N-4} &\to B^R_{N-3} \\ &. \end{aligned} \tag{69}$$

4. Now, we start from $n = 1$ and sweep to right. Renew $B^L_2, B^L_3, \cdots, B^L_{N/2}$ by this procedure.

$$\begin{aligned} B^L_1 \bullet\bullet B^R_{N-3} &\to B^L_2 \\ B^L_2 \bullet\bullet B^R_{N-4} &\to B^L_3 \\ &\vdots \\ B^L_{N/2-1} \bullet\bullet B^R_{N/2-1} &\to B^L_{N/2} \end{aligned} \tag{70}$$

5. Go back to 2) and repeat the procedure until the calculation converges.

2.3 Fukui-Hatsugai-Suzuki Method

In the practical numerical calculation, since there are two partial differentiations exist in the definition of Chern number, it seems that we need to prepare a very dense mesh when we discretize the Brillouin zone. However, by using this method, it is possible to calculate a Chern number by calculating only for discretized points of the Brillouin zone without worrying about a gauge choice.

A Chern number for a Hamiltonian $\hat{\mathcal{H}}(k_1, k_2)$ of integer quantum Hall system is expressed as follows:

$$c_n = \frac{1}{2\pi i} \int_0^{2\pi} dk_1 \int_0^{2\pi} dk_2 F(k_1, k_2), \tag{71}$$

$$F(k_1, k_2) = \partial_1 A_2 - \partial_2 A_1, \tag{72}$$

$$A_\mu = \langle n|\partial_\mu|n\rangle\,. \tag{73}$$

To evaluate this by the numerical calculation straightforwardly, we should discretize the Brillouin zone by meshes and calculate a difference instead of differential. In this way, we need very dense mesh. Therefore, we use a method introduced by Fukui, Hatsugai, and Suzuki[44]. In Fukui-Hatsugai-Suzuki method, we also divide the Brillouin zone into meshes, and then calculate a $U(1)$ link variable on each edge, and field strength on each plaquette, and calculate the Chern number by summing up all the field strengths.

Now we look up the procedure of Fukui-Hatsugai-Suzuki method closely. First, divide the parameter space $k_1, k_2 \in [0, 2\pi]$ to $n \times n$ mesh. The edge length of each plaquet will be $a = 2\pi/n$. Then, we define a $U(1)$ link variable as follows:

$$\begin{aligned} U_\mu(\mathbf{k}) &= \langle n(\mathbf{k})|n(\mathbf{k} + a\hat{\mathbf{e}}_\mu)\rangle \,/N_\mu(\mathbf{k}), & (74)\\ N_\mu(\mathbf{k}) &= |\langle n(\mathbf{k})|n(\mathbf{k} + a\hat{\mathbf{e}}_\mu)\rangle|\,, & (75)\\ \mathbf{k} &= (k_1, k_2), \quad (\mu = 1, 2). & (76) \end{aligned}$$

Here, $\mathbf{e}_1$ and $\mathbf{e}_2$ are unit vectors in the k_1 and k_2 direction. From this link variable, we define field strength $\tilde{F}_{12}(\mathbf{k})$ and lattice Chern number $\tilde{c}_n$.

$$\tilde{F}_{12}(\mathbf{k}) = \ln U_1(\mathbf{k})U_2(\mathbf{k} + a\hat{\mathbf{e}}_1)U_1(\mathbf{k} + a\hat{\mathbf{e}}_2)^{-1}U_2(\mathbf{k})^{-1}, \tag{77}$$

$$-\pi < \frac{1}{i}\tilde{F}_{12}(\mathbf{k}) \leqq \pi, \tag{78}$$

$$\tilde{c}_n = \frac{1}{2\pi i}\sum_k \tilde{F}_{12}(\mathbf{k}). \tag{79}$$

$\tilde{c}_n$ only takes integer values. In the limit of infinitesimally small plaquettes, $\tilde{c}_n$ coincides with normal definition of Chern number. Therefore, if we take the plaquettes sufficiently small, we obtain a correct Chern number. More precisely, it is proper when a condition

$$|F_{12}(\mathbf{k})|\delta k_1 \delta k_2 \approx |\tilde{F}_{12}(\mathbf{k})| < \pi \quad \text{for all } \mathbf{k} \tag{80}$$

is satisfied.

2.4 Time-dependent Schrödinger equation

To simulate the Thouless pumping in a continuum model, we need to solve a time-dependent Schrödinger equation. Euler method, which is the simplest method to solve a first degree differential equation, is numerically unstable. Therefore, we need

to use a numerically stable method which can reduce the calculation time. In this research, we use a method initiated by M. Tsukada[45].

The outline of this method is explained by next three points:

1. The state is developed in each very short time Δt. This makes it possible to adjust any kind of Hamiltonian, including a time-dependent Hamiltonian.

$$|\psi(t+\Delta t)\rangle = \exp[-\mathrm{i}\Delta t\mathcal{H}]|\psi(t)\rangle \tag{81}$$

2. Cayley form is used to guarantee the numerical stability.

$$\exp[-\mathrm{i}\Delta t\mathcal{H}] \simeq \frac{1-\mathrm{i}\Delta t\mathcal{H}/2}{1+\mathrm{i}\Delta t\mathcal{H}/2} \tag{82}$$

3. An exponential product decomposition is used for the time evolution operator.

$$\exp[-\mathrm{i}\Delta t\mathcal{H}] \simeq \prod_n \exp\left[-\mathrm{i}\Delta t\mathcal{H}_n\right] \tag{83}$$

To explain this method, we start from a 1D Schrödinger equation for a free particle below.

$$\mathrm{i}\frac{\partial}{\partial t}\psi(x,t) = -\frac{1}{2}\frac{\partial^2}{\partial x^2}\psi(x,t) \tag{84}$$

When we know a wave function at time t, we can obtain a wave function after a very short time by multiplying the time evolution operator. The formal solution can be written as:

$$\psi(x,t+\Delta t) = \exp\left[\mathrm{i}\frac{\Delta t}{2}\frac{\partial^2}{\partial x^2}\right]\psi(x,t). \tag{85}$$

To make the calculation numerically stable, we use Cayley form, which is unitary.

$$\psi(x,t+\Delta t) \simeq \frac{1+\mathrm{i}\Delta t\partial_x^2/4}{1-\mathrm{i}\Delta t\partial_x^2/4}\psi(x,t) \tag{86}$$

Also, we need to discretize a spacial variable. A spatial partial differentiation operator is expressed as:

$$\frac{\partial^2}{\partial x^2}\psi\left(x_i\right) \simeq \frac{\psi\left(x_{i+1}\right) - 2\psi\left(x_i\right) + \psi\left(x_{i-1}\right)}{\Delta x^2}. \tag{87}$$

At first sight, an inverse matrix appears in Eq. (86), hence the computational complexity is $\mathcal{O}(N^3)$. However, it can be reduced to $\mathcal{O}(N)$ as follows.

We should solve a simultaneous equation below:

$$\begin{pmatrix} A & -1 & 0 & \dots & 0 \\ -1 & A & -1 & & \vdots \\ 0 & -1 & A & \ddots & 0 \\ \vdots & & \ddots & \ddots & -1 \\ 0 & \cdots & 0 & -1 & A \end{pmatrix} \begin{pmatrix} \psi\left(x_1, t+\Delta t\right) \\ \psi\left(x_2, t+\Delta t\right) \\ \psi\left(x_3, t+\Delta t\right) \\ \vdots \\ \psi\left(x_N, t+\Delta t\right) \end{pmatrix} = \begin{pmatrix} B & -1 & 0 & \dots & 0 \\ -1 & B & -1 & & \vdots \\ 0 & -1 & B & \ddots & 0 \\ \vdots & & \ddots & \ddots & -1 \\ 0 & \cdots & 0 & -1 & B \end{pmatrix} \begin{pmatrix} \psi\left(x_1, t\right) \\ \psi\left(x_2, t\right) \\ \psi\left(x_3, t\right) \\ \vdots \\ \psi\left(x_N, t\right) \end{pmatrix}, \tag{88}$$

where

$$A \equiv \frac{4\Delta x^2}{\mathrm{i}\Delta t} + 2, \quad B \equiv \frac{4\Delta x^2}{\mathrm{i}\Delta t} - 2. \tag{89}$$

To solve this, we execute next four steps.

1. Define an auxiliary vector $\mathbf{b}$.
   For $i = 1, \ldots, N-1$
   $$b_i = \psi_{i-1} + B\psi_i + \psi_{i+1}. \tag{90}$$

2. Applying the recursion formula forward.
   For $i = 1, \ldots, N-1$
   $$b_i = (b_i + b_{i-1})\, u_i. \tag{91}$$

3. Applying the recursion formula backward.
   For $i = N-2, \ldots, 1$
   $$b_i = b_i + b_{i+1} u_i. \tag{92}$$

4. Replacing ψ by b_i.
   For $i = 1, \ldots, N$
   $$\psi_i = b_i. \tag{93}$$

The calculation amount of each steps is $\mathcal{O}(N)$.

Next, we consider a 2D time-dependent Schrödinger equation:

$$\mathrm{i}\frac{\partial}{\partial t}\psi(\mathbf{r}, t) = -\frac{1}{2}\left[\frac{\partial^2}{\partial x^2} + \frac{\partial^2}{\partial y^2}\right]\psi(\mathbf{r}, t). \tag{94}$$

A formal expression of time evolution operator is

$$\psi(\mathbf{r}, t + \Delta t) = \exp\left[\mathrm{i}\frac{\Delta t}{2}\left(\frac{\partial^2}{\partial x^2} + \frac{\partial^2}{\partial y^2}\right)\right]\psi(\mathbf{r}, t). \tag{95}$$

Since each spatial partial differentiation is commutative, the time evolution operator can be written as:

$$\psi(\mathbf{r}, t + \Delta t) = \exp\left[\mathrm{i}\frac{\Delta t}{2}\frac{\partial^2}{\partial x^2}\right]\exp\left[\mathrm{i}\frac{\Delta t}{2}\frac{\partial^2}{\partial y^2}\right]\psi(\mathbf{r}, t). \tag{96}$$

Therefore, it can be calculated independently for each axis in turn, by using the same technique as Eq. (88) $\sim$ Eq. (93).

Finally, we consider a 2D time-dependent Schrödinger equation with potential term:

$$\mathrm{i}\frac{\partial}{\partial t}\psi(\mathbf{r}, t) = \left(-\frac{\triangle}{2} + V(\mathbf{r})\right)\psi(\mathbf{r}, t), \tag{97}$$

where

$$\triangle \equiv \frac{\partial^2}{\partial x^2} + \frac{\partial^2}{\partial y^2}. \tag{98}$$

In this case, the time evolution operator is

$$\psi(\mathbf{r}, t + \Delta t) = \exp\left[-\mathrm{i}\Delta t\left(-\frac{\triangle}{2} + V(\mathbf{r})\right)\right]\psi(\mathbf{r}, t). \tag{99}$$

By using an exponential product decomposition, it can be written as:

$$\psi_i(\mathbf{r}, t + \Delta t) \simeq \exp\left[i\frac{\Delta t}{2}\frac{\triangle}{2}\right]\exp[-i\Delta t V(\mathbf{r})]\exp\left[i\frac{\Delta t}{2}\frac{\triangle}{2}\right]\psi_i(\mathbf{r}, t). \tag{100}$$

This formula can be derived by using Baker-Campbell-Hausdorff formula. This formula enables it to calculate the time evolution by multiplying an exponential term one by one, as we have done in (96).

Chapter 3 Topological Properties of Ultracold Bosons in One-Dimensional Quasiperiodic Optical Lattice

In this chapter, we introduce a one-dimensional (1D) Bose-Hubbard model with a quasiperiodic superlattice potential and analyze its topological properties. First, in Sec. 3.1, we explain the backgrounds of quasicrystals and 1D quasiperiodic model. In Sec. 3.2, we define the model Hamiltonian. Our methods for numerical analysis of the model our definition of the topological number in 1D quasiperiodic models are given in Sec. 3.3. After that, the basic topological properties of the Harper-type Bose-Hubbard model are shown in Sec. 3.4. Finally, in Sec. 3.5, we investigate whether a topological equivalence between Harper-type and Fibonacci-type models exists even in the interacting system. A brief summary of our findings concludes this chapter in Sec. 3.6.

3.1 Backgrounds

3.1.1 Quasicrystals

Various materials forming quasicrystals have been studied for their unique physical properties[46, 47, 48, 49, 50]. In recent years, topological phases have been a focus of constant attention in condensed matter physics[51, 52]. A typical example of topological phase is the integer quantum Hall effect, where the quantized Hall conductance is proportional to the Chern number[3]. The 1D version of a quasicrystal is a quasiperiodic lattice. The relation between one-dimensional quasiperiodic systems and two-dimensional topological insulators has recently been pointed out[53] and experimentally confirmed by using optical waveguides[54]. This idea provides a new point of view for both quasicrystals and topological phases[55, 56, 57]. Accordingly, a detailed analysis for topological phases in quasicrystals is needed.

3.1.2 1D Quasiperiodic model

Next, we explain the topological equivalence which is proper to 1D quasiperiodic systems. Kraus *et al.* proved that some sort of 1D quasiperiodic models are toplogically

equivalent[58]. Consider the Hamiltonian as follows:

$$\hat{\mathcal{H}} = \sum_n \left[(-t + \lambda^{\mathrm{od}} V_n^{\mathrm{od}}) c_n^\dagger c_{n+1} + \mathrm{H.c.} + \lambda^{\mathrm{d}} V^{\mathrm{d}} c_n^\dagger c_n\right]. \tag{101}$$

Here, V^{od} and V^{d} are quasiperiodic. There are two well-known 1D quasiperiodic models, Harper model and Fibonacci model. In Harper model, we use $V_{\mathrm{Harper}} = \cos(2\pi bn)$, and in Fibonacci model, we use $V_{\mathrm{Fibonacci}} = 2(\lfloor b(n+2)\rfloor - \lfloor b(n+1)\rfloor) - 1$ for the quasiperiodic function. Figures 3.1 and 3.2 are a schematic diagram of Harper model and Fibonacci model. As the figure shows, in Harper model, site-dependent potential takes various values, making V_{Harper} quasiperiodic, but in Fibonacci model, $V_{\mathrm{Fibonacci}}$ only takes two values, and its order is quasiperiodic. Kraus *et al.* proposed a function which connects V_{Harper} and $V_{\mathrm{Fibonacci}}$ smoothly:

$$V_{\mathrm{S}} = \frac{\tanh\{\beta[\cos(2\pi bn + \phi) - \cos \pi b]\}}{\tanh \beta}. \tag{102}$$

Here, the parameter β changes between 0 and ∞. This function becomes Harper model in the limit of $\beta \to 0$, and Fibonacci model in the limit of $\beta \to \infty$. We can also make a new quasiperiodic model by changing a potential modulation λ^{d} and hopping modulation λ^{d}. Kraus *et al.* showed that the energy gap does not close when the β, $\lambda^{\mathrm{od}}/\lambda^{\mathrm{d}}$ changes their values in the range of $[0, \infty]$, which implies that those are topologicaly equivalent.

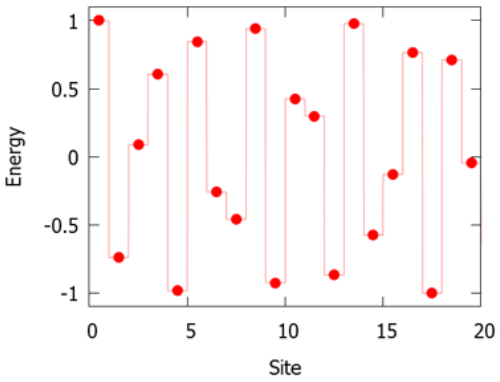

Figure 3.1: Harper-type potential.

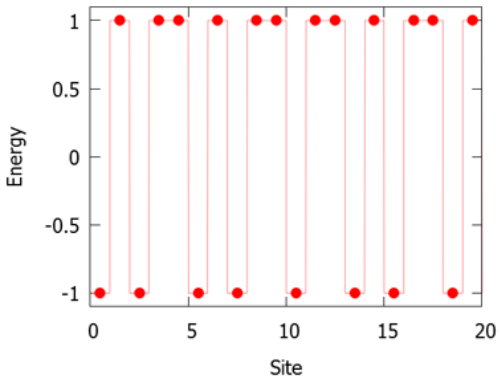

Figure 3.2: Fibonacci-type potential.

1D quasiperiodic models have theoretically been studied in various contexts[4, 59, 60, 61]. 1D quasiperiodic systems can be realized not only by using optical waveguides, but also by using ultracold atoms[28, 62, 63]. An important difference between optical waveguide systems and ultracold atomic systems is the existence of tunable particle-particle interactions. In the optical waveguide systems, photons do

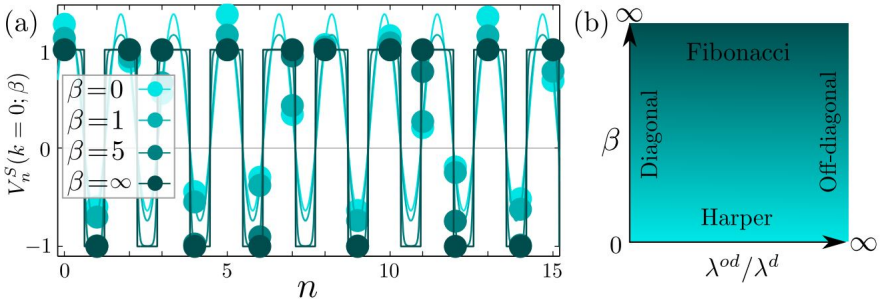

Figure 3.3: (a) Function which connects Harper model and Fibonacci model smoothly. (b) Range where topological equivalence is ensured in 1D quasiperiodic system. Citation from [58].

not interact with each other, but in the ultracold atomic systems, it is possible to introduce and control the strength of interaction by using Feshbach resonance[64]. Such advances have stimulated theoretical studies of 1D quasiperiodic systems with interaction[65, 66, 67, 68, 69, 70, 71, 72, 73, 74, 75, 76, 77, 78, 79]. Kraus *et al.* showed that two different types of 1D quasicrystals can be smoothly connected without gap closing, which implies their topological equivalence[58].

3.2 Model

We investigate the topological properties of the Bose-Hubbard model with quasiperiodic modulation described by the Hamiltonian defined on an L-site chain,

$$\hat{\mathcal{H}}(\phi,\beta) = -t\sum_{\langle j,j'\rangle}\left(\hat{b}_{j'}^{\dagger}\hat{b}_j + \text{H.c.}\right) + \sum_j\left[\lambda V\left(\phi,j\right)\hat{n}_j + \frac{U}{2}\hat{n}_j(\hat{n}_j+1)\right], \tag{103}$$

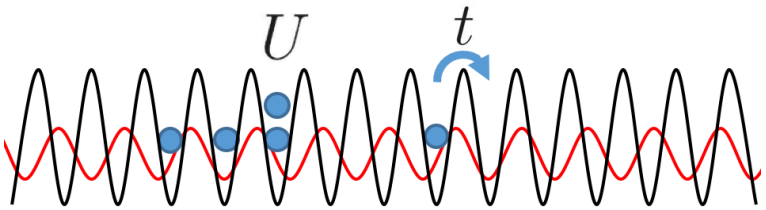

Figure 3.4: Bose-Hubbard model with quasiperiodic modulation.

which $\hat{b}_j^{\dagger}(\hat{b}_j)$ is the boson creation (annihilation) operator, $\hat{n}_j = \hat{b}_j^{\dagger}\hat{b}_j$ is the particle number operator, t is the hopping strength, λ is the modulation strength of quasiperiodic potential, ϕ is the phase of the modulation, U is the on-site interaction strength, $V\left(\phi,j\right)$ are periodic functions of j with period $(2\pi b)^{-1}$. The hopping is introduced

between neighboring sites ($j' = j+1, j = 0, \ldots, (L-2)$), and also between the end sites ($(j, j') = (L-1, 0)$) with a phase factor $e^{i\theta}$ for the $\hat{b}_1^\dagger \hat{b}_L$ term for the twisted boundary condition (see below). In the following we take $t = 1$ as the unit of energy.

3.3 Methods

We apply the exact diagonalization and the density matrix renormalization group (DMRG) method to numerically obtain the many-body ground state of Eq. (103) for a given number N of bosons. In order to investigate the topological properties of this system, we analyze the effect of boson number change in the open boundary condition and also calculate the Chern number by introducing twisted boundary conditions. The Chern number (with respect to (θ, ϕ)) is defined as

$$C = \frac{1}{2\pi i} \int_0^{2\pi} d\theta \int_0^{2\pi} d\phi \left[\left\langle \frac{d\Psi}{d\theta} \middle| \frac{d\Psi}{d\phi} \right\rangle - \left\langle \frac{d\Psi}{d\phi} \middle| \frac{d\Psi}{d\theta} \right\rangle \right] \tag{104}$$

in which θ is the phase of the twisted boundary condition. However, it is not possible to introduce twisted boundary conditions on a finite system with a genuine quasiperiodicity, because a quasiperiodic system does not have translation symmetry. Thus, we approximate the irrational number b, which characterizes the quasiperiodicity of the system, by a rational number so that we may impose twisted boundary conditions. We obtain the best rational approximations of the irrational number b by using convergents of continued fraction representations. For example, for

$$b = \frac{3-\sqrt{5}}{2} = 1 - \cfrac{1}{1 + \cfrac{1}{1 + \ldots}}, \tag{105}$$

the rational approximations will be 1/2, 1/3, 2/5, 3/8, 5/13, and so on. Additionally, we have used the method for calculating the Chern number from the ground states for a discrete set of values of (θ, ϕ).[44] In DMRG, we must use the same basis for four values of parameters forming a rectangle in the (θ, ϕ)-space to calculate link variables and lattice field strength which is defined in Ref.[44].

3.4 Topological Properties of the Harper-type Bose-Hubbard model

1D Bose-Hubbard model can be boiled down to a one-particle problem of spinless fermions in the hard-core limit ($U = \infty$) by using a Jordan-Wigner transformation such as

$$\hat{b}_j^\dagger = \hat{c}_j^\dagger \prod_{n=1}^{j-1} e^{i\pi \hat{c}_n^\dagger \hat{c}_n}. \tag{106}$$

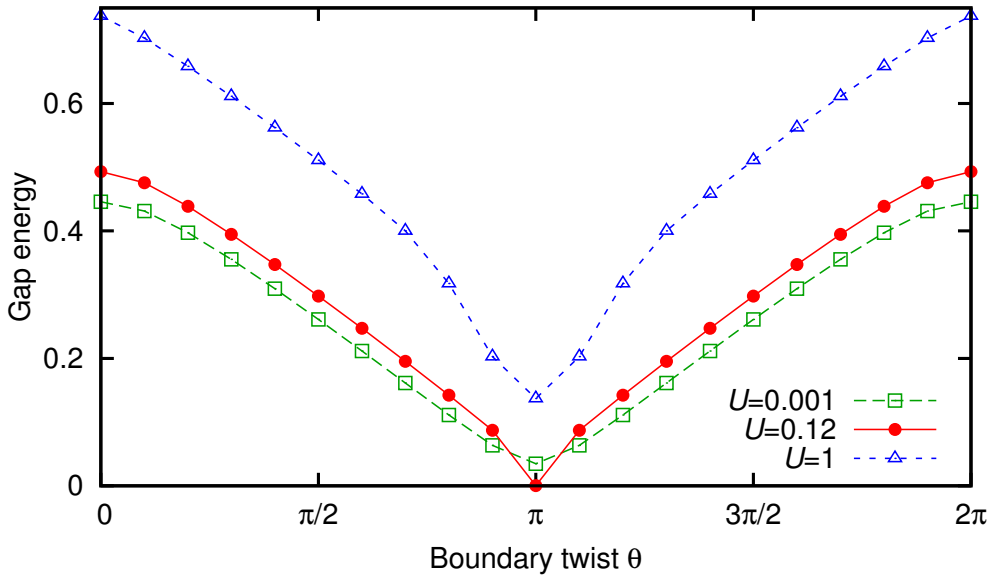

Figure 3.5: Energy gap plotted as a function of θ in $[0, 2\pi]$, $\phi = 0$ plotted for three strengths of the interaction $U = 0.001, 0.12, 1.0$; $\lambda = 1$, $(L, N) = (8, 3)$ for $b = 3/8$.

For the diagonal ($V^{\mathrm{od}} = 0$) Harper-type modulation $V^{\mathrm{d}}(\phi, j) = \cos(2\pi bj + \phi)$, the new Hamiltonian is

$$\hat{\mathcal{H}} = -t \sum_{\langle jj' \rangle} (\hat{c}_{j'}^{\dagger} \hat{c}_j + \mathrm{H.c.}) + \lambda \sum_j \cos(2\pi bj + \phi) \hat{n}_j, \tag{107}$$

in which $\hat{c}_j^{\dagger}(\hat{c}_j)$ is the fermion creation (annihilation) operator and $\hat{n}_j = \hat{c}_j^{\dagger} \hat{c}_j$. When $b = p/q$ with coprime integers p and q, which means that b is rational, the system is periodic with a period q. In this condition, the energy band splits into q bands. This band structure conforms with that of the electrons on square lattice under magnetic fields. When b is irrational, the band structure will be a cantor set and every band gap has a non-trivial Chern number[5].

Now, we consider the case with a finite U. First, we approximate the quasiperiodic system by a periodic system (see (3)). When U is sufficiently large, the system is similar to a free fermion system, and the gap energy will be close to the single particle level separation at the Fermi level in the fermion system. When U is sufficiently small, almost all of the particles are in the one-particle ground state. Between these limits, we observe that the energy gap between the ground state and the first excited state closes for a certain choice of (θ, ϕ) at a number of values of U. The gap closing behavior is shown in Fig. 3.5 for an approximate system of $b = 3/8$. This result is consistent with the previous studies of Bose-Hubbard model with a periodic superlattice, in which topological transitions are observed[80, 81].

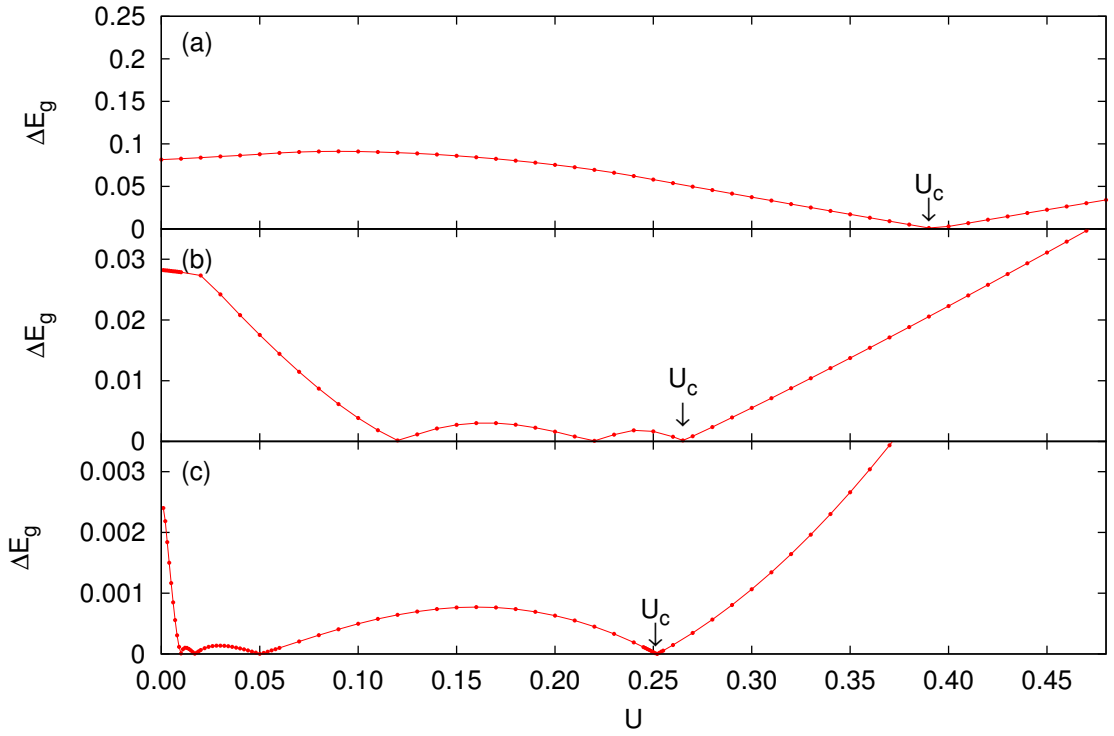

Figure 3.6: The minimum energy gap ΔE_g in the (θ, ϕ) space plotted as a function of U for $t = 1$, $\lambda = 1$. (a): $b = 2/5$, $(L, N) = (5, 2)$. (b): $b = 3/8$, $(L, N) = (8, 3)$. (c): $b = 5/13$, $(L, N) = (13, 5)$. $U_c \simeq 0.39, 0.27, 0.25$ for (a), (b), and (c) respectively.

What happens as we improve the approximation of the quasiperiodicity in Eq.(3)? Fig. 3.6 shows ΔE_g, which is the minimum of the energy gap between the ground state and the first excited state, in the parameter range $\phi \in [0, 2\pi), \theta \in [0, 2\pi)$ for $b = 2/5, 3/8, 5/13$. When the energy gap is zero for a certain choice of (θ, ϕ), or ΔE_g becomes zero, the topological number is allowed to change its value. We define U_c as the largest U when the gap closes. We also calculate the Chern number. If $U < U_c$, the Chern number takes various values often changing by multiples of L. However, if $U > U_c$, for which the gap energy monotonically increases when U increases. The Chern number remains $C = 1$ in all accuracies $b = 2/5, 3/8, 5/13$. This indicates that it is topologically non-trivial in the limit of quasiperiodic system $(b \to (3 - \sqrt{5})/2)$.

In non-interacting fermionic systems, topologically protected edge states arise when the Chern number is non-zero and the system has an open boundary condition. This phenomenon is called the bulk-edge correspondence. In a 1D quasiperiodic

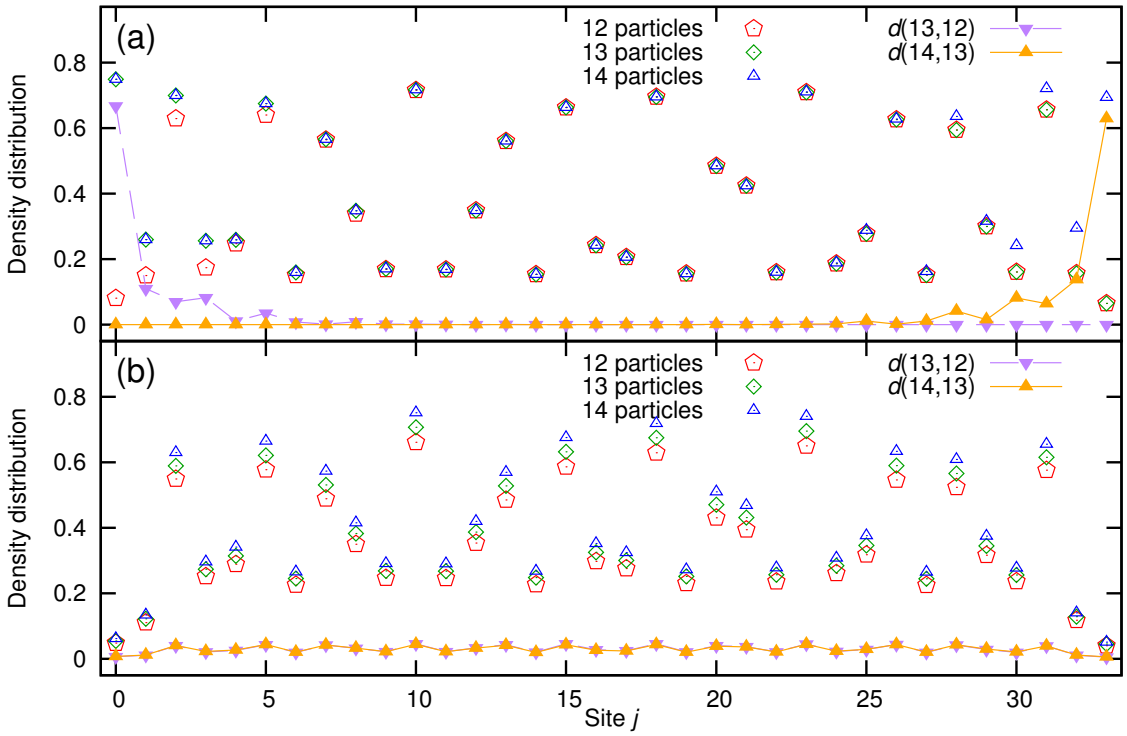

Figure 3.7: The difference between the particle density distribution of the ground state of quasiperiodic Bose-Hubbard model with 34 sites, $b = \frac{\sqrt{5}-1}{2}$, $\phi = 2$, $\lambda = 1$ and filling $\nu = 12/34, 13/34, 14/34$, (a) $U = 100$ and (b) 1. Red, green, blue points respectively show the particle density distribution $n_N(j)$ of N-particle systems for $N = 12, 13, 14$, and purple and orange lines show the difference between them, $d(N+1, N) \equiv n_{N+1}(j) - n_N(j)$ for $N = 12, 13$.

system, such a topologically protected state arises as an end state, which is a localized state at the end of the system. In contrast, in interacting bosonic systems, we find that a non-trivial topological character appears in the particle density distribution. In our system, when the interaction strength U is sufficiently large, such a localization can be seen in the difference in the density distribution between the ground states of different fillings, which is shown in Fig. 3.7, calculated by DMRG in the open boundary condition.

The edge localization structure appears only in particular ranges of ϕ. The range of ϕ where the edge localized structure can be seen depends on the system size, as in non-interacting fermion systems. This adiabatic pumping might be detected by using the method proposed in Ref. [82], by observing the center of mass after pumping for several cycles. However, as U becomes smaller, the edge localized structure smoothly disappears, and the localization structure is not observed for any ϕ when

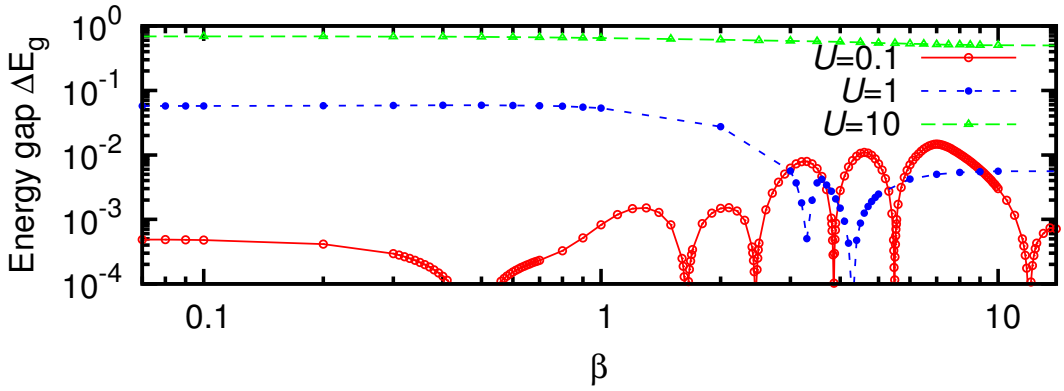

Figure 3.8: The minimum energy gap between the ground state and the first excited state for the system of 13 sites with open boundary condition, $b = 5/13$, $U = 0.1$, 1 and 10, $\lambda = 1$. When U is sufficiently large, while β changes, the gap remains open and the topological number is fixed. This implies that Harper-like Bose-Hubbard model and Fibonacci-like Bose-Hubbard model are topologically equivalent in large U region.

U is sufficiently small. We show a typical profile in Fig. 3.7. Despite the edge structure being absent in whole range of ϕ, the Chern number remains non-zero. This implies that the edge localization structure does not have the same property as in the edge mode in non-interacting fermionic systems. Similar non-local density difference has been observed in the topologically non-trivial insulating phase in a superlattice Bose-Hubbard system[83].

3.5 Harper model and Fibonacci model

Now we demonstrate that the ground states of the Harper-type and Fibonacci-type Bose-Hubbard models can be smoothly connected without closing the energy gap ΔE_g when the interaction is moderately strong. This implies that these two models are topologically equivalent. According to Ref. [58], we define a smooth modulation

$$V(\phi, j, \beta) = \frac{\tanh\left[\beta\left(\cos\left(2\pi b j + \phi\right) - \cos\left(\pi b\right)\right)\right]}{\tanh\beta}, \tag{108}$$

which becomes a Harper (Fibonacci) type one in the limit of $\beta \to 0$ ($\beta \to \infty$). Using this smooth modulation function, we consider the Hamiltonian as follows:

$$\begin{aligned}\hat{\mathcal{H}}(\phi, \beta) = &- t \sum_{\langle jj' \rangle} \left(\hat{b}^{\dagger}_{j'} \hat{b}_j + \text{H.c.}\right) \\ &+ \sum_j \left[\lambda V\left(\phi + 3\pi b, j, \beta\right) \hat{n}_j + \frac{U}{2} \hat{n}_j (\hat{n}_j + 1)\right].\end{aligned} \tag{109}$$

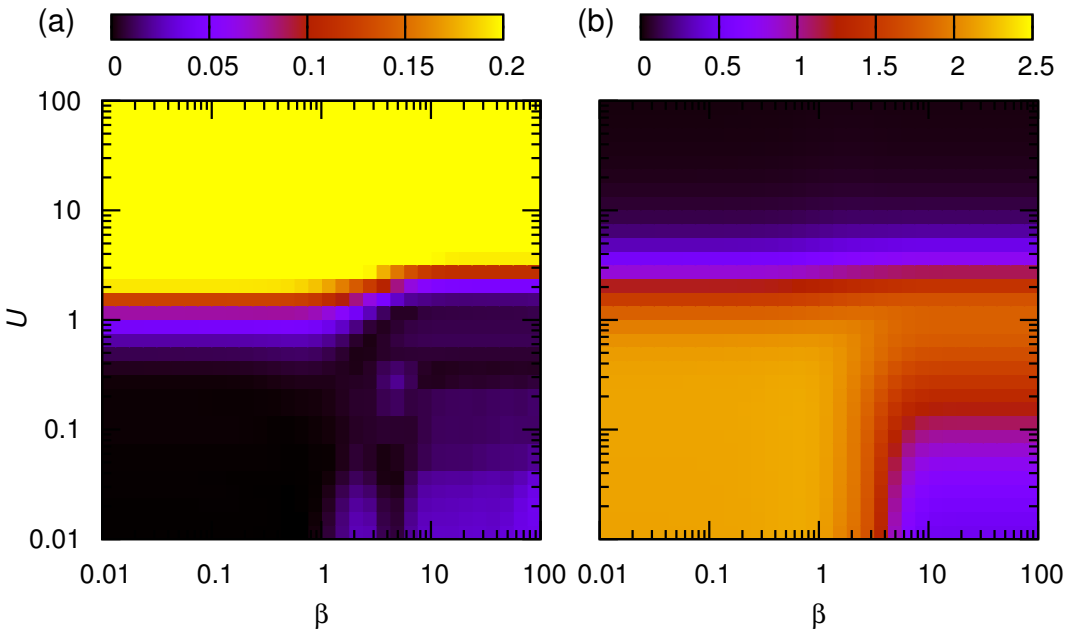

Figure 3.9: (a) The minimum energy gap and (b) the superfluid density as a function of U and β computed for a system with (a) $b = 5/13$, $(L, N) = (13, 5)$, $\lambda = 1$, (b) $b = 8/21$, $(L, N) = (21, 8)$, $\lambda = 1$. Superfluid density is calculated for fixed phase $\phi = 0$.

We investigate the behavior of the energy gap ΔE_g while the parameters β and U changes. Figure 3.8 shows the energy gap ΔE_g as a function of β. Since ΔE_g does not become zero while β changes for $U = 10$, we conclude that the Harper-type and Fibonacci-type Bose-Hubbard models are topologically equivalent. The gap-closing behaviors for smaller U are different. When $U = 1$ and $U = 0.1$, ΔE_g becomes zero two and six times respectively. This behavior is complicated and sensitive to U. These gap-closing behaviors arise from finite size effects in the superfluid phase as discussed later.

To investigate the phase diagram as a function of β and U, we plot the energy gap ΔE_g and superfluid density ρ_s in Fig. 3.9. The energy gap ΔE_g is calculated by taking the minimum of the excitation energy as we did in Fig. 3.5. The superfluid (SF) density can be computed using twisted boundary conditions:

$$\rho_s = 2\pi L \frac{E_0^{\text{apbc}} - E_0^{\text{pbc}}}{\pi^2}, \tag{110}$$

which is defined in Ref. [66], where E_0^{pbc} and E_0^{apbc} are the ground state energies for periodic ($\theta = 0$) and anti-periodic ($\theta = \pi$) boundary conditions. The SF density does

not strongly depend on ϕ. As β is changed, U_c changes its value. In the Harper-type region ($\beta \sim 0$), $U_c \sim 0.25$ in this approximation accuracy as we mentioned. However, in the Fibonacci-type region ($\beta \sim \infty$), $U_c \sim 1.55$.

According to Ref. [66], in the Harper-type quasiperiodic Bose-Hubbard model, there are three phases in the quasiperiodic Bose-Hubbard model when the particle number density matches b, namely superfluid (SF), Bose glass (BG), and incommensurate charge density wave (ICDW). Figure 3.9(b) shows the superfluid density for $\phi = 0$. We have checked that the value of the superfluid density is almost unchanged even if we change the phase ϕ.This plot suggests that SF phase emerges at low U and low β region. At low U and high β region, the superfluid density is almost zero, but the energy gap is very small. These properties conform with the BG phase. The rest of the region ($U > U_c(\beta)$) is a gapful phase, which is ICDW. The shape of the ICDW region can be found from the region with the relatively-large energy gap in Fig. 3.9. The above results support that this phase has a non-trivial Chern number $C = 1$, and that the whole ICDW region is topologically equivalent.

3.6 Summary

To summarize, we have considered a quasiperiodic Bose-Hubbard model with interaction by using exact diagonalization and DMRG. First, we have shown that the energy gap of the Harper-type Bose-Hubbard model increases as the on-site interaction strength U increases when $U > U_c$ ($\sim 0.25t$), and at the same time, topological number (Chern number) stays non-zero and constant. Also, while the topological equivalence between quasiperiodic models such as the Harper model and the Fibonacci model was only known in non-interacting fermionic systems previously, here we have shown that the topological equivalence exists also between interacting quasiperiodic systems, the Harper-type and Fibonacci-type Bose-Hubbard models. The equivalence exists when U is moderately large, and the boundary of topologically non-trivial phase has been revealed. Moreover, the phase diagram as a function of β and U has been investigated. The phase diagram includes superfluid, Bose glass, and incommensurate charge density wave.

Chapter 4 Two-Dimensional Thouless Pumping of Ultracold Fermions in Obliquely Introduced Optical Superlattice

In this chapter, we propose a two-dimensional (2D) square lattice model with an obliquely introduced superlattice of ultracold atomic system, where a 2D version of Thouless pumping can be realized. First, in Sec. 4.1, we explain the backgrounds of our proposal. In Sec. 4.2, we introduce a 2D square lattice tight-binding model with various types of obliquely introduced potential, a single well and a superlattice. Next, we consider a continuum model with obliquely introduced superlattice and analyze its topological nature in Sec. 4.3. We investigate the effect of a harmonic trap by solving the time-dependent Schrödinger equation in Sec. 4.4. Finally, Sec. 4.5 summarize this chapter.

4.1 Backgrounds

Intensive studies of the quantum Hall effect have opened up a wide research area which is known as topological phases [51, 52]. Topological phases are characterized by the associated invariants, which are prohibited to vary unless the energy gap closes. Moreover, topological phases have a characteristic property called the bulk-edge correspondence[84, 85, 86, 52], which guarantees the existence of the edge states, meaning that electrons can only move on the edge of a given material, as far as the bulk topological invariant has a non-trivial value. In quantum Hall systems, the topological invariant is defined by the Chern number[4, 87, 88, 89], and it appears as the quantized Hall conductance. Similar relationships also appear in 3D quantum Hall systems[90, 91, 92, 93].

Topological phases can be realized in various experimental platforms, not only in materials, but also in optical waveguides[54], photonic systems[94, 95, 96], etc. In particular, a great amount of efforts have been made to realize topological insulators

in cold atom systems by using synthetic gauge fields, which are induced by an optical lattice[97]. Various topological systems have been realized in cold atom systems, for instance, the Su-Schriefer-Heeger model [27], the Hofstadter model [98, 99], synthetic dimensions [36, 37], and the Haldane model [28]. Recently, topological charge pumping which is called Thouless pumping[2, 100] has been realized in cold atom systems [25, 101], and also many theoretical proposals have been made in numerous studies[102, 103, 104, 82, 105, 106, 107, 108, 109, 110, 111, 112, 26, 113, 114, 115, 116, 117]. Also, 2D Thouless pumping, where the nonlinear response is characterized by 4D topological invariant, is realized in Ref. [118].

Mapping Hamiltonian between different dimensions plays an important role in understanding topological properties. One of the significant examples of mapping can be seen in the problem of Hofstadter butterfly[5]. Hofstadter mapped a two-dimensional (2D) system of square lattice under a uniform magnetic field to a 1D equation, which is called the Harper equation. Interestingly, a recent research of Thouless pumping used this mapping backwards, and showed the topological equivalence over a certain group of Hamiltonians. This kind of mapping to higher dimensions can be applied not only to 1D systems, but also to two and higher dimensional systems[57].

Recently, the development of experimental techniques regarding cold atoms in optical lattice is remarkable[119, 120], and the degree of freedom in designing the quantum simulation is high. Triangle[10], square[121], and hexagonal lattices[122] have all been realized in cold atom systems. Moreover, it is possible to realize non-standard lattices in cold atom systems. One example of such lattices is the lattice made by superimposing a usual lattice potential and a superlattice potential. For example, in Ref.[123], Taie *et al.* realized an optical Lieb lattice by adding a diagonal lattice to a usual square optical lattice. By taking advantage of these high degrees of freedom of the optical lattice, various topological phases are proposed theoretically[124, 125, 126, 127, 128, 129, 130, 131, 132] and realized experimentally[133, 134, 135, 136, 137, 138]. In particular, the cold atom system is one of the most suitable platforms for realizing Thouless pumping. Various types of Thouless pumping are realized in cold atom experiments[25, 101, 139, 118].

Also, this chapter is partly motivated by recent remarkable progress in solid state physics, i.e. twisted bilayer graphene (TBG). TBG is receiving a lot of attention lately because of the realization of unconventional superconductivity[140]. TBG has been investigated in many contexts, such as its electronic structures[141, 142], flat bands[143], topological band structures[144], and Moiré butterflies[145]. It provides also a prototypical example of superimposed lattice potential.

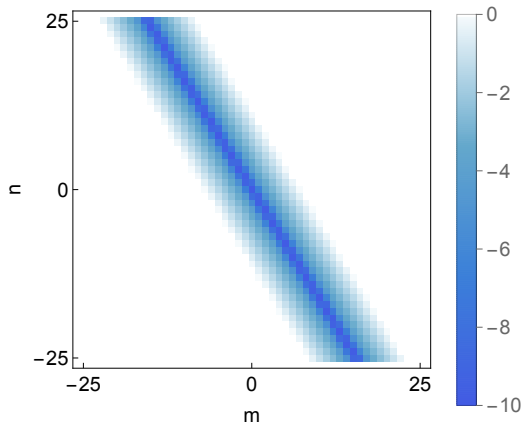

Figure 4.1: Plot of on-site potential in the case of $\boldsymbol{a} = (\frac{\sqrt{5}+1}{2}, 1)$, $V(x) = -Ve^{-x^2/w^2}$, $V = 10$, $w = 1$, $\delta = 0$. Horizontal and vertical axes correspond to m and n directions respectively.

4.2 Tight-binding Model

4.2.1 Model

Stimulated by the above mentioned previous studies, it is natural to ask what happens if the additional diagonal lattice in the optical Lieb lattice is angled. Here, as a paradigmatic example, we consider a fermion gas loaded in the 2D optical square lattice with a superlattice structure which is introduced obliquely. The lattice constant is taken to be unity. We study the topological properties of the system which is described by the following Hamiltonian:

$$\begin{aligned} \hat{\mathcal{H}} = & \sum_{m,n} \left[-t \left(\hat{c}^\dagger_{m+1,n} \hat{c}_{m,n} + \hat{c}^\dagger_{m,n+1} \hat{c}_{m,n} \right) + \text{H.c.} \right] \\ & + \sum_{m,n} \left[V_{m,n} \hat{c}^\dagger_{m,n} \hat{c}_{m,n} \right], \qquad (111) \\ V_{m,n} = & \, V(d), \qquad (112) \\ d = & \, \frac{\boldsymbol{a}}{|\boldsymbol{a}|} \cdot \begin{pmatrix} m - \delta \\ n \end{pmatrix}, \qquad (113) \end{aligned}$$

where $\hat{c}^\dagger_{m,n}(\hat{c}_{m,n})$ is the fermion creation (annihilation) operator, t is the hopping strength, δ is the parameter of the real-space potential shift, $\boldsymbol{a} = (a_x, a_y)$ is the normal vector of the superlattice direction, and d implies the distance from the line which is expressed by $a_x(x - \delta) + a_y y = 0$. The boundary conditions are taken either open or periodic. Below we take $t = 1$ as the unit of energy.

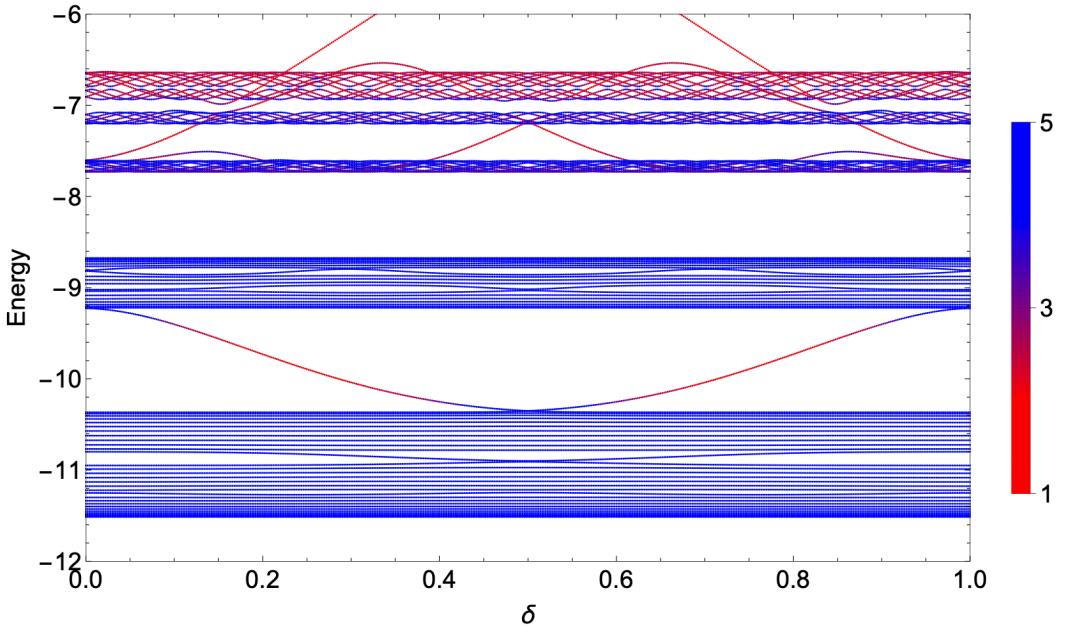

Figure 4.2: Energy spectrum plotted against the parameter δ, which represents to what extent the obliquely introduced potential is shifted spatially. The on-site potential is given in Fig. 4.1, with open boundary conditions. The bulk of the spectrum remains unchanged, with a few of the states crossing across the band gap. The color shows the PR, which measures the spread of the eigenfunction.

4.2.2 Obliquely Introduced Single Well

First, we consider the case that $V(d)$ has a single dip, where the Hamiltonian has an oblique linear-shaped single well. We take $V(d) = -Ve^{-d^2/w^2}$, $\boldsymbol{a} = (\frac{\sqrt{5}+1}{2}, 1)$ as the linear-shaped potential, which restricts particles to move around the potential in the low-energy region. The on-site potential in this system is plotted in Fig. 4.1. As a consequence of the overlap of the square lattice and obliquely introduced potential, this model can be effectively considered as a 1D tight-binding model with a superlattice. This effective superlattice opens the energy gap. By the analogy to the previous studies of topological aspects of 1D superlattice[53, 54], the edge states will appear when we drive the phase of the superlattice, which corresponds to the parameter δ in this model. In Fig. 4.2, we diagonalize the tight-binding model, which is described in Eq. (111), with the system size 50×50 and under the open boundary condition. Figure 4.2 shows the plots for the bottom part of the energy spectrum since the upper part of the spectrum has no band gap because of the 2D nature of the wave function. We can see the existence of band-crossing states in the energy spectrum with open boundary conditions as a function of δ in Fig. 4.2. The color in

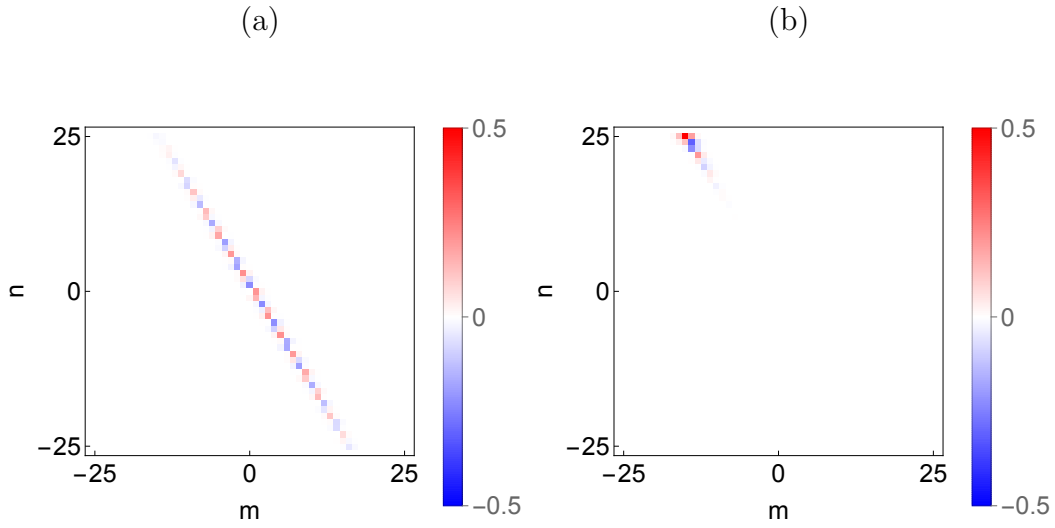

Figure 4.3: Wave functions of the energy eigenstate in the xy plane: (a) 30th and (b) 31st excited state in real space with $\delta = 0.75$. While the wave functions are spread over the oblique potential in (a), they are localized at the edge in (b). Horizontal and vertical axes correspond to m and n directions respectively.

the figure shows the participation ratio (PR) which is defined as

$$I_\psi = \left(\sum_{m,n} |\psi_{m,n}|^4 \right)^{-1}. \tag{114}$$

Small PR denotes that the eigenfunction is well localized. Note that the bulk band is fixed because we choose an irrational number for tangent α. Figures 4.3 (a) and (b) show the wave function of an in-band state and a band-crossing state. We confirm that the wave function of the band-crossing state is localized around the edge.

With changing $\boldsymbol{a}$, the distribution of energy band also changes. Figure 4.4 shows the energy spectrum plotted against a tilting angle θ, which is related to $\boldsymbol{a}$ through the formula $\boldsymbol{a} \propto (\cos\theta, \sin\theta)$. We diagonalize the tight-binding model with the system size 50×50 and under the open boundary condition. For the same reason as in Fig. 4.2, Fig. 4.4 shows the plots only for the bottom part of the energy spectrum. As shown in the figure, a butterfly-like structure appears in the energy spectrum plot. This structure is similar to the "3D butterfly" which is introduced in Refs. [92, 93]. We will explain the origin of this similarity later. The color in Fig. 4.4 represents PR in each eigenfunction, which is defined in Eq. Eq. (114). We can see that the eigenstates in the band gap are well localized, corresponding to edge states in topological systems.

The upper part of Figure 4 also shows many localized states, but this is not the point we want to focus on because the wave functions in this region are no longer

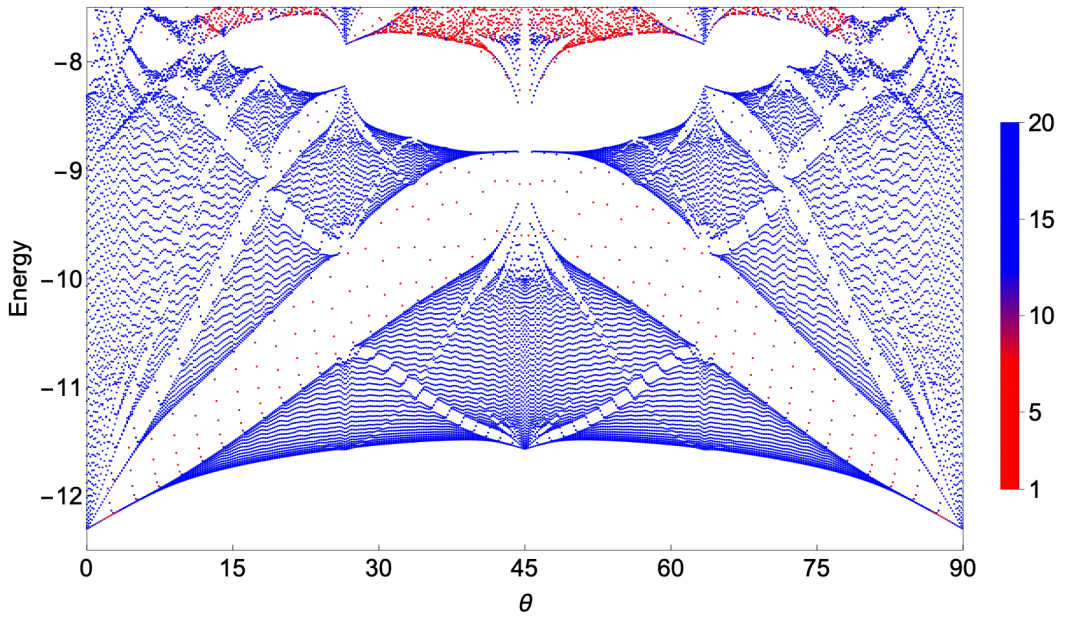

Figure 4.4: Butterfly structure in plots of the energy spectrum against the tilting angle θ in the case of $\boldsymbol{a} = (\cos\theta, \sin\theta)$, $V(x) = -Ve^{-x^2/w^2}$, $V = 10$, $w = 1$, $\delta = 0$. The color shows PR which is defined in Eq. (114).

quasi-one-dimensional.

4.2.3 Obliquely Introduced Superlattice

As we have seen in the previous section, the band crossing states and the edge localized states appear when $V(d)$ is a single well, exemplifying the topological nature of the effective 1D system. We will now discuss topological properties in 2D when $V(d)$ is a periodic function. As a typical periodic function, we take $V(d) = V\cos(\lambda d)$. In this case, when we vary δ slowly, the Hamiltonian will be periodic in time, and this setup corresponds to the adiabatic transport, which was first proposed by Thouless[2].

It is known that the mapping between a 1D superlattice system and a 2D Hofstadter model exists[58]. Analogously, we can clearly understand the topological aspects of our model by mapping it to a 3D Hamiltonian. For simplicity, we start our discussion in the case that a_x/a_y is a rational number. The Hamiltonian can be

rewritten as follows:

$$\begin{aligned}
&\mathcal{H}(\phi) \\
&= -t \sum_{m,n} \left[\hat{c}^{\dagger}_{m+1,n}(\phi)\hat{c}_{m,n}(\phi) + \hat{c}^{\dagger}_{m,n+1}(\phi)\hat{c}_{m,n}(\phi) + \text{H.c.} \right] \\
&+V \sum_{m,n} \cos\left(2\pi \left(\frac{p_x}{q_x} m + \frac{p_y}{q_y} n \right) + \phi \right) \hat{c}^{\dagger}_{m,n}(\phi)\hat{c}_{m,n}(\phi),
\end{aligned} \tag{115}$$

where q_x and q_y determine the period for x and y direction of the Hamiltonian, respectively. Also, we use $\phi \equiv 2\pi\delta p_x/q_x$ for the parameter controlling the phase of the cosine-type potential. We can map this Hamiltonian to a 3D Hamiltonian by using Fourier transformation,

$$\hat{c}_{m,n}(\phi) = \frac{1}{\sqrt{2\pi L_z}} \sum_l e^{-il\phi} \hat{c}_{m,n,l} \tag{116}$$

$$\hat{c}_{m,n,l} = \frac{1}{\sqrt{2\pi L_z}} \sum_l e^{il\phi} \hat{c}_{m,n}(\phi). \tag{117}$$

Hamiltonian Eq. (115) will be

$$\begin{aligned}
\mathcal{H}_{\text{3D}} \quad &= -t \sum_{m,n,l} \left[\hat{c}^{\dagger}_{m+1,n,l}\hat{c}_{m,n,l} + \hat{c}^{\dagger}_{m,n+1,l}\hat{c}_{m,n,l} + \text{H.c.} \right] \\
&+ \frac{V}{2} \sum_{m,n,l} \left[e^{2\pi i \left(\frac{p_x}{q_x} m + \frac{p_y}{q_y} n \right)} \hat{c}^{\dagger}_{m,n,l+1}\hat{c}_{m,n,l} + \text{H.c.} \right].
\end{aligned} \tag{118}$$

This Hamiltonian describes a 3D tight-binding model on the cubic lattice with a homogeneous magnetic field, whose direction is perpendicular to the z-axis but oblique in the xy-plane. There are previous studies for this model, and it is known that the Hofstadter butterfly and the integer quantum Hall effect (IQHE) also appear in the 3D lattice[90, 91, 92, 93]. According to Refs. [92, 93], each gap in the 3D Hofstadter butterfly is characterized by two Chern indices. In the 3D model, these indices are proportional to the Hall conductivity. When we go back to our 2D model, these indices determine the topological pumping just like Thouless pumping, and the bulk-edge correspondence shows that the pumped amount and the number of edge states match each other. In this model, pumped amount in x-direction and y-direction corresponds to the number of localized states at edges of x-direction and y-direction, respectively. Also, by comparing Eq. (115) and Eq. (118), we can see that potential strength V corresponds to the hopping strength in the z-direction. These correspondences explain why the 3D butterfly appears in Fig. 4.4.

Here we have only considered a cosine-type potential, but a similar mapping is also possible for other types of potentials for which there are higher frequency components, and these components will be mapped to longer distance hoppings in the z-direction.

4.2.4 Diophantine Equation

By mapping the Hamiltonian, we have seen that the Chern number characterizes the system, but how does the Chern number appear in observables? This question can be solved by considering the polarization. Since the derivative of the polarization is proportional to the current, the pumped amount is proportional to the total amount of change in the polarization. Now, let us briefly summarize the theory of polarization.

According to Ref. [146], the polarization has an integer ambiguity by a multiple of the lattice constant, but the change of the polarization in the course of a continuous change of the Hamiltonian can be defined without ambiguity. When we write the wave vector of the electronic wave function $\mathbf{k} = (k_x, k_y)$, the change of the polarization can be written as

$$\Delta \mathbf{P}_{\mathbf{i}\to\mathbf{f}} = \int_{\mathbf{i}}^{\mathbf{f}} (\partial_\phi \mathbf{P})\, d\phi \tag{119}$$

$$\partial_\phi \mathbf{P} = \frac{e}{S} \sum_n^{\text{occ}} \int_{\text{BZ}} 2\,\text{Im}\,\langle \partial_\phi \psi_{n\mathbf{k}} | \partial_{\mathbf{k}} \psi_{n\mathbf{k}} \rangle\, d^2k \tag{120}$$

where ϕ is the parameter of the Hamiltonian, S is the area of the Brillouin zone, and the charge of an electron is $-e$. This integrand has the same form of expression as the Berry curvature[1].

Following the above formula for the change of the polarization, we can define the pumped amount even in infinite systems. Namely an analogy with Eqs. (119) and (120) enables us to express the pumped amount in x and y-direction for our 2D system when ϕ is increased from $\phi_\text{i} = 0$ to $\phi_\text{f} = \phi$ as:

$$P_x(\phi) = -\int_0^\phi d\phi' \frac{a_y}{2\pi} \int_{-2\pi/a_y}^{2\pi/a_y} dk_y \frac{a_x}{2\pi} \int_{-2\pi/a_x}^{2\pi/a_x} dk_x 2\,\text{Im}\,\langle \partial_{\phi'} \psi_{nk_x} | \partial_{k_x} \psi_{nk_x} \rangle \tag{121}$$

$$P_y(\phi) = -\int_0^\phi d\phi' \frac{a_y}{2\pi} \int_{-2\pi/a_y}^{2\pi/a_y} dk_y \frac{a_x}{2\pi} \int_{-2\pi/a_x}^{2\pi/a_x} dk_x 2\,\text{Im}\,\left\langle \partial_{\phi'} \psi_{nk_y} | \partial_{k_y} \psi_{nk_y} \right\rangle . \tag{122}$$

In the presence of the superlattice potential, the lattice periodicity is multiplied by q_x and q_y for x and y-direction respectively. Therefore, the size of the first Brillouin zone shrinks by $(1/q_x) \times (1/q_y)$. This can be regarded as an analog of the magnetic Brillouin zone[1]. We note that the signs in Eqs. (121) and (122) are opposite to the counterpart in Eq. (120) due to the sign of an electron charge.

[1] In our model, the inversion symmetry is restored when one of the sites is on the minimum line of the potential. Since there are $q_x q_y$ sites in the superlattice produced by the on-site potential, there are $q_x q_y$ points protected by inversion symmetry in one cycle in our model.

Considering the case where ϕ is periodic with period 2π, the pumped amount in x and y-direction in one period for our 2D system is written as:

$$P_x(2\pi) = -\frac{a_y}{2\pi}\int_{-2\pi/a_y}^{2\pi/a_y} dk_y \left[\frac{a_x}{2\pi}\int_0^{2\pi} d\phi \int_{-2\pi/a_x}^{2\pi/a_x} dk_x 2\,\mathrm{Im}\,\langle \partial_\phi \psi_{nk_x} | \partial_{k_x}\psi_{nk_x}\rangle\right] \tag{123}$$

$$P_y(2\pi) = -\frac{a_x}{2\pi}\int_{-2\pi/a_x}^{2\pi/a_x} dk_x \left[\frac{a_y}{2\pi}\int_0^{2\pi} d\phi \int_{-2\pi/a_y}^{2\pi/a_y} dk_y 2\,\mathrm{Im}\,\langle \partial_\phi \psi_{nk_y} | \partial_{k_y}\psi_{nk_y}\rangle\right]. \tag{124}$$

The formula in the square brackets in Eqs. (123) and (124) has the same form as the definition of the Chern number on the torus created by (ϕ, k_x) and (ϕ, k_y), respectively. The Chern number is guaranteed to be an integer, but $P_x(P_y)$ is not necessarily an integer, because it is given by the average of Chern numbers. However, if changing $k_y(k_x)$ does not close the band gap, then the Chern number does not change either, so $P_x(P_y)$ is also an integer. To summarize, in an adiabatic time-periodic system, the amount pumped in the x-direction during one period is represented by the integral of the change in polarization in the x-direction, which corresponds to the average in the k_y-direction of the Chern numbers for (ϕ, k_x).

As we have mentioned above, in the tight-binding approximation, we can map our model to a 3D cubic lattice model with an obliquely introduced homogeneous magnetic field in Eq. (118), and the amount of Thouless pumping in our model corresponds to the quantized Hall conductance in the cubic lattice model. In Eq. (118), x and y are cyclic coordinates, so that the wave function can be written as $\Psi_{lmn} = e^{ik_x m + ik_y n} F_l$, where k_x and k_y are the Bloch wave numbers along the x and y directions. Then the Schrödinger equation will be

$$t(F_{l-1} + F_{l+1}) - V\{\cos(2\pi l p_x/q_x + k_x) + \cos(2\pi l p_y/q_y + k_y)\}F_l = EF_l. \tag{125}$$

This equation is equivalent to a 3D version of the Harper equation. By analyzing this equation, the following Diophantine equation can be obtained [91],

$$\frac{r}{Q} = s + u\frac{p_x}{q_x} + v\frac{p_y}{q_y}. \tag{126}$$

Here, r is the number of filled bands and Q is the least common multiple of q_x and q_y. u and v correspond to the pumped amount while φ changes from 0 to $2\pi/Q$. The details of the derivation of this equation is shown in the next section.

Below we focus on the case where $p_x = p_y = 1$ and q_x, q_y are coprime. Then Eq. (126) can be transformed to

$$r \equiv uq_y + vq_x \ (\mathrm{mod}\ Q). \tag{127}$$

q_x	2	3	2	3	4	2	3	4	5	6
q_y	3	4	5	5	5	7	7	7	7	7
u	1	1	1	-1	1	1	1	-1	-2	1
v	-1	-1	-2	2	-1	-3	-2	2	3	-1

Table 4.1: Several examples of the solution of the Diophantine equation Eq. (145) with the smallest absolute value in the case of $p_x = p_y = 1$, $r = 1$.

Basically, we are concerned with the lowest band, so we should consider the case $r = 1$. Table 4.2.4 shows the solution of Eq. (145) in several cases.

We show the details of the derivation of this equation below.

4.2.5 Derivation of Diophantine Equation in Tight-Binding Limit

Here, we derive Eq. (126) from the Hamiltonian,

$$\begin{aligned}\mathcal{H}(\phi) = & t_x \sum_{m,n} \left[\hat{c}^\dagger_{m+1,n}(\phi)\hat{c}_{m,n}(\phi) + \text{h.c.}\right] \\ & + t_y \sum_{m,n} \left[\hat{c}^\dagger_{m,n+1}(\phi)\hat{c}_{m,n}(\phi) + \text{h.c.}\right] \\ & + V \sum_{m,n} \cos\left(2\pi\left(\Phi_x m + \Phi_y n\right) + \phi\right) \hat{c}^\dagger_{m,n}(\phi)\hat{c}_{m,n}(\phi).\end{aligned} \tag{128}$$

This Hamiltonian is periodic in ϕ with period 2π. Here, we suppose that Φ_x and Φ_y are rational numbers, such as $\Phi_x = p_x/q_x, \Phi_y = p_y/q_y$, where (p_x, q_x) and (p_y, q_y) are pairs of coprime integers with $q_x, q_y > 0$.

The Fourier-transformed Hamiltonian obtained by using Eq. (118) is

$$\begin{aligned}H = -\int_{-\pi}^{\pi} \frac{dk_x}{2\pi} \int_{-\pi}^{\pi} \frac{dk_y}{2\pi} \Bigg[& t\left(\cos\left(k_x\right) + \cos\left(k_y\right)\right) \hat{c}^\dagger(k_x, k_y, k_z)\hat{c}(k_x, k_y, k_z) \\ & + \frac{V}{2}\Big(e^{-ik_z}\hat{c}^\dagger(k_x + 2\pi\Phi_x, k_y + 2\pi\Phi_y, k_z)\hat{c}(k_x, k_y, k_z) \\ & + e^{ik_z}\hat{c}^\dagger(k_x - 2\pi\Phi_x, k_y - 2\pi\Phi_y, k_z)\hat{c}(k_x, k_y, k_z)\Big)\Bigg].\end{aligned} \tag{129}$$

Here, we have defined $k_z = \phi$ for convenience. However, there is a mixing between $(k_x, k_y, k_z) \to (k_x \pm 2\pi\Phi_x, k_y \pm 2\pi\Phi_y, k_z)$ and thus the Hamiltonian is not diagonal in $\mathbf{k}$. To diagonalize this, we need to separate k_x, k_y into $q_x \times q_y$ regions as follows,

$$k_x = k_x^0 + 2\pi\Phi_x m, \tag{130}$$

$$k_y = k_y^0 + 2\pi\Phi_y n. \tag{131}$$

Then, the Hamiltonian can be written as:

$$H = \frac{1}{(2\pi)^3}\int_{-\pi/q_x}^{\pi/q_x} dk_x^0 \int_{-\pi/q_y}^{\pi/q_y} dk_y^0 \int_{-\pi}^{\pi} dk_z \hat{H}(k_x^0, k_y^0, k_z), \tag{132}$$

$$\begin{aligned}\hat{H}(k_x^0, k_y^0, k_z) = \sum_{m=0}^{q_x-1}\sum_{n=0}^{q_x-1} \Big\{ & -2t\left(\cos\left(k_x^0 + 2\pi\Phi_x m\right) + \cos\left(k_y^0 + 2\pi\Phi_y n\right)\right) \\ & \times \hat{c}^\dagger\left(k_x^0 + 2\pi\Phi_x m, k_y^0 + 2\pi\Phi_y n, k_z\right)\hat{c}\left(k_x^0 + 2\pi\Phi_x m, k_y^0 + 2\pi\Phi_y n, k_z\right) \\ & -\frac{V}{2}\Big(e^{-ik_z}\hat{c}^\dagger\left(k_x^0 + 2\pi\Phi_x(m+1), k_y^0 + 2\pi\Phi_y(n+1), k_z\right)\hat{c}\left(k_x^0 + 2\pi\Phi_x m, k_y^0 + 2\pi\Phi_y n, k_z\right) \\ & + e^{ik_z}\hat{c}^\dagger\left(k_x^0 + 2\pi\Phi_x(m-1), k_y^0 + 2\pi\Phi_y(n-1), k_z\right)\hat{c}\left(k_x^0 + 2\pi\Phi_x m, k_y^0 + 2\pi\Phi_y n, k_z\right)\Big)\Big\}.\end{aligned} \tag{133}$$

Note that the Brillouin zone is reduced to $[-\pi/q_x, \pi/q_x]$ for k_x and $[-\pi/q_y, \pi/q_y]$ for k_y. Now, the Schrödinger equation $\hat{H}\left(k_x^0, k_y\right)|\psi\rangle = E_{k_x^0,k_y}|\psi\rangle$ is reduced to that for a 1D tight-binding model. The single particle energy is obtained by expanding the state into single-particle states at each lattice point m,

$$|\psi\rangle = \sum_{m=0}^{q-1} a_m \hat{c}^\dagger(k_x^0 + 2\pi\Phi_x m, k_y^0 + 2\pi\Phi_y m, k_z)|0\rangle, \tag{134}$$

where $|0\rangle$ is the vacuum. The eigenvalue equation is

$$\begin{aligned}\left(-2t\cos\left(k_x^0 + 2\pi\Phi_x n\right) - 2t\cos\left(k_y^0 + 2\pi\Phi_y n\right)\right)a_n \\ -\frac{V}{2}\left(e^{-ik_z}a_{n-1} + e^{ik_z}a_{n+1}\right) = E_{k_x^0,k_y^0,k_z}a_n.\end{aligned} \tag{135}$$

This corresponds to the Harper equation for the Hofstadter model. Let Q be the least common multiple of q_x and q_y, and let N_x and N_y be integers which satisfy $N_x/Q = p_x/q_x = \Phi_x$, $N_y/Q = p_y/q_y = \Phi_y$. For convenience, we perform the transformation

$$a_j = \sum_{l=0}^{Q-1} e^{i2\pi jl/Q} b_l, \tag{136}$$

and we obtain

$$\begin{aligned}& -t_x\left(e^{ik_x^0}b_{j+N_x} + e^{-ik_x^0}b_{j-N_x}\right) \\ & -t_y\left(e^{ik_y^0}b_{j+N_y} + e^{-ik_y^0}b_{j-N_y}\right) \\ & -V\cos\left(k_z + \frac{2\pi j}{Q}\right)b_j = E_{k_x^0,k_y^0,k_z}b_j.\end{aligned} \tag{137}$$

To solve this equation, we apply the perturbation theory under the condition $t_x, t_y \ll V$. The solution at $t_x, t_y = 0$ is

$$E_m\left(k_x^0, k_y^0, k_z\right) = -2t_a\cos\left(k_z + \frac{2\pi m}{Q}\right), \quad \psi_j = \delta_{j,m}. \tag{138}$$

If we make t_x, t_y finite, gaps open at the degeneracy points. To understand the details, we should make the condition for degeneracy clear. When the two bands ψ_{m_1} and ψ_{m_2} cross each other, the degeneracy condition is

$$k_z + \frac{2\pi}{Q} m_1 = -\left(k_z + \frac{2\pi}{Q} m_2 \right) \pmod{2\pi}. \tag{139}$$

The degeneracy only occurs when $k_z = 0, \pm\pi/q$, so we can rewrite it as

$$m_1 + m_2 + l \equiv 0 \pmod{q} \quad (l \in \{0, \pm 1\}, l = q k_x^0/\pi). \tag{140}$$

It is obvious that the lowest band corresponds to $m = 0$. It is possible to determine all of the band indices by using Eq. (140). There is a simple relation between the gap number r and band indices m_1, m_2,

$$r \equiv -|m_1 - m_2| \pmod{Q}. \tag{141}$$

Now we are ready to use the perturbation theory. Since the $t_x(t_y)$ term only mixes two sites which are $P_x(P_y)$ sites apart from each other, in order to hybridize ϕ_{m_1} and ϕ_{m_2}, the following equation must be satisfied,

$$|m_1 - m_2| = N_x t_r + N_y u_r \pmod{Q}, \tag{142}$$

that is,

$$\frac{r}{Q} = s_r + \frac{p_x}{q_x} u_r + \frac{p_y}{q_y} v_r. \tag{143}$$

The lowest order of perturbation which mixes ϕ_{m_1} and ϕ_{m_2} is the $|u_r|$th order for the t_x term, and $|v_r|$th order for the t_y term, respectively.

The Hamiltonian around the rth gap is

$$\begin{pmatrix} \epsilon & \Delta e^{-ik_x u_r} e^{-ik_y v_r} \\ \Delta e^{ik_x u_r} e^{ik_y v_r} & -\epsilon \end{pmatrix} \begin{pmatrix} a \\ b \end{pmatrix} = E \begin{pmatrix} a \\ b \end{pmatrix}. \tag{144}$$

Now, it is possible to calculate the amount of pumping in one cycle from this Hamiltonian. The pumped amount will be t_r for x-direction and u_r for y-direction, and this is exactly the solution of Diophantine equation Eq. (143). However, we should be aware that "one cycle" here corresponds to the width of Brilliouin zone of k_z, while k_z changes its value by $2\pi/Q$.

Below we focus on the case where $p_x = p_y = 1$ and q_x, q_y are coprime. Then Eq. (126) can be transformed to

$$r \equiv u q_y + v q_x \pmod{Q}. \tag{145}$$

Basically, we are concerned with the lowest band, so we should consider the case $r = 1$. Table 4.2.4 shows the solution of Eq. (145) in several cases.

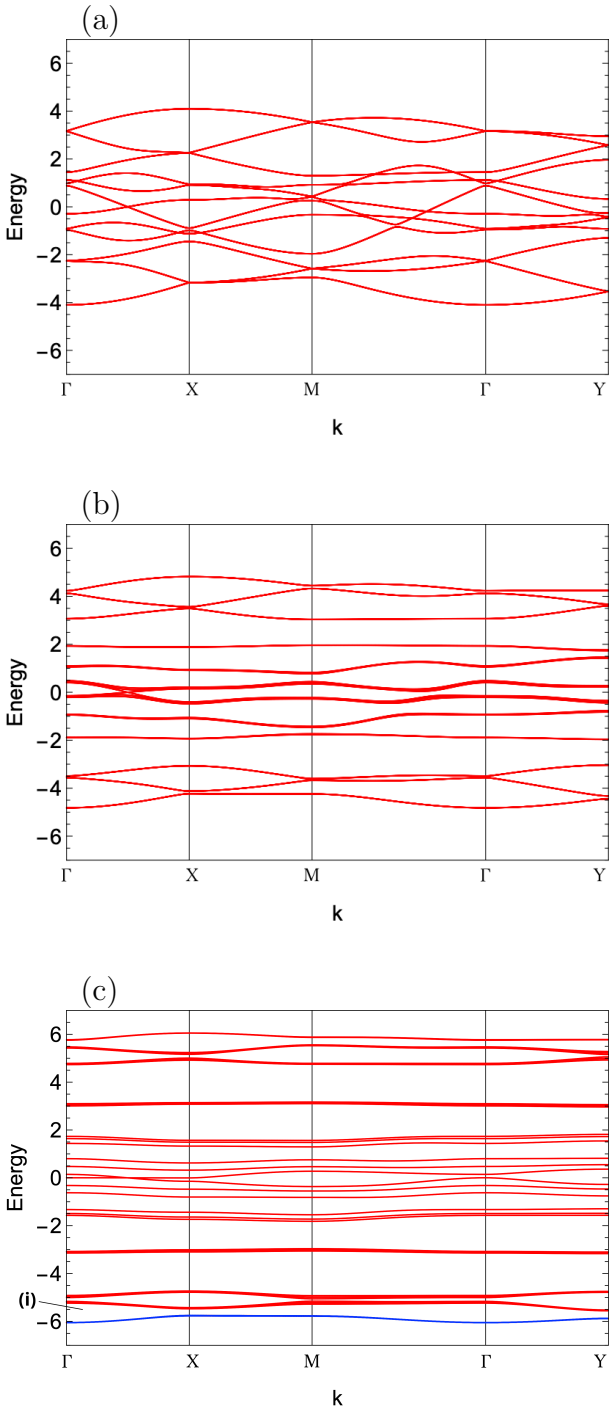

Figure 4.5: Band structure computed using the tight-binding approximation with $q_x = 3, q_y = 4$ and (a)$V = 1.0$, (b) $V = 3.0$, and (c) $V = 5.0$, respectively. The blue band in (c) corresponds to the lowest band and the symbol (i) indicates the lowest band gap. The high-symmetry points in the first Brillouin zone are defined as $\Gamma = (0, 0), X = (\pi, 0), Y = (0, \pi)$, and $M = (\pi, \pi)$.

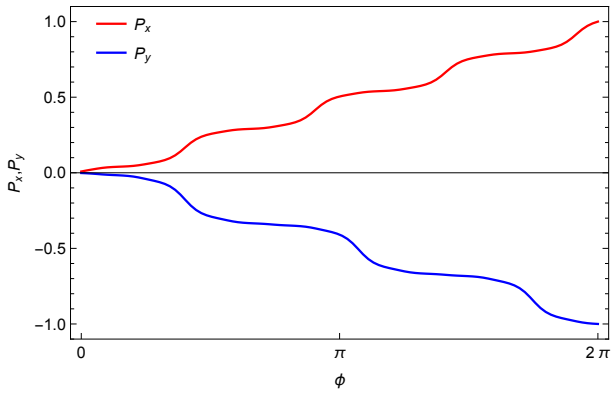

Figure 4.6: The pumped amount which is calculated by integrating the Berry curvature and using the tight-binding approximation with $q_x = 3, q_y = 4, V = 5.0$.

4.2.6 Band Structure and Pumped Amount

In the previous section, we have shown that the pumped amount obeys the Diophantine equation. Now we show a concrete example below. In particular, we focus on the case $q_x = 3, q_y = 4$.

Figure 4.5 shows how the band changes when the magnitude of the modulation V of the onsite potential is changed. Figures 4.5 (a), (b) and (c) are the band structure for $V = 1.0, 3.0, 5.0$ respectively. When V is large, the lowest band gap (i) is opened, which can be observed in Fig. 4.5 (c). On the contrary, when V is small, the Berry curvature could not be calculated well since the band gap is small. The smaller the band gap, the larger number of meshes are required for the Fukui-Hatsugai-Suzuki method. The reason why the band gap is so small is that the higher order perturbations open the gap. It is not likely that the band gap is closed in the process of increasing V, so it seems that the gap is open even if V is very small, but is too small to be detected numerically.

Here we investigate the pumped amount for the lowest band in Fig. 4.5 (c). We apply the Fukui-Hatsugai-Suzuki method[44] in order to calculate the pumped amount, which can be obtained by integrating the Berry curvature[1]. The specific expression of the pumped amount is given in Eqs. (121) and (122). Figure 4.6 shows the pumped amount for large V, which is calculated by using Eqs. (121) and (122). The pumped amount after one cycle, $P_x = 1$ and $P_y = -1$, agrees with the solution of the Diophantine equation shown in Table 4.2.4.

4.3 Continuum model

4.3.1 Model

In the light of the analogy of Thouless pumping and IQHE, the results in the previous section suggest that the amount of transport, as the Hamiltonian parameter ϕ changes its value from 0 to 2π, is quantized and can be expressed in terms of the Chern number. Since the discussion in the previous section is based on the tight-binding model, it is desirable to extend our discussion to continuum systems so as to apply the results to cold atom systems. To treat the system more precisely and to see the feasibility of the previous model in the experimental setups, let us consider next a 2D continuum model.

To be specific, we consider the following Hamiltonian,

$$\begin{aligned} H_{\rm cont} &= \int dxdy\psi^\dagger(x,y)\Big[-\frac{\hbar^2}{2m}\frac{\partial^2}{\partial x^2}-\frac{\hbar^2}{2m}\frac{\partial^2}{\partial y^2} \\ &\qquad + V_x(x,y)+V_y(x,y)+V_{\rm SL}(x,y)\Big]\psi(x,y), \quad (146) \\ V_j(x,y) &= 2V_j\cos(q_j j) \quad (j=x,y), \quad (147) \\ V_{\rm SL}(x,y) &= 2V_{\rm SL}\cos(p_x x+p_y y-\varphi), \quad (148) \end{aligned}$$

where $\psi(x,y)$ is the field operator of a particle, $\hbar$ is Planck's constant, and m is the mass of a particle. There are three types of potentials in this system: V_x, V_y, and $V_{\rm SL}$. V_x and V_y form the 2D square lattice, and $V_{\rm SL}$ forms the superlattice oblique to the square lattice.

4.3.2 Band Structure

We now apply the plane-wave approximation to the Hamiltonian introduced in Eqs. (146) $\sim$ (148) to calculate the eigenenergies and the wave functions directly. First, we apply Fourier-transformation:

$$\psi_{k_x,k_y}=\frac{1}{\sqrt{L_xL_y}}\int dxdye^{ik_xx+ik_yy}\psi(x,y), \quad (149)$$

to Eq. (146). Then, we obtain the following Hamiltonian.

$$\begin{aligned} H=\sum_{0\le k_x,k_y<1}\sum_{n_x,n_y=-\infty}^{\infty}\Big[&\frac{1}{2}\left((k_x+n_x)^2+(k_y+n_y)^2\right)\psi^\dagger_{n_xn_y}\psi_{n_xn_y} \\ &+\left(V_x\psi^\dagger_{n_xn_y}\psi_{n_x+q_x,n_y}+V_y\psi^\dagger_{n_xn_y}\psi_{n_x,n_y+q_y}+V_{\rm SL}e^{-i\varphi}\psi^\dagger_{n_xn_y}\psi_{n_x+p_x,n_y+p_y}+{\rm H.c.}\right)\Big]. \end{aligned} \quad (150)$$

When the condition $V_x, V_y, V_{\rm SL} \ll 1$ is satisfied, it is possible to diagonalize Eq. (150) numerically by introducing the cutoff for wavenumbers k_x and k_y.

Figure 4.7 shows the band structure when the plane-wave approximation is used. To calculate the wave function under the plane-wave approximation, we introduce the cut-off of wave number k. To be specific, we only consider small n_x and n_y satisfying the condition: $|n_x|, |n_y| \leqq 12$ in Eq. (150). The band structure is similar to that of Fig. 4.5 when $V_{\rm SL}$ is small, but the gap begins to increase as $V_{\rm SL}$ increases, and the first gap is clearly open in the plot for $V_{\rm SL} = 0.5$. Even in this model, it is unlikely that a phase transition accompanied by the gap formation occurs somewhere, so we expect that a gap opens even if $V_{\rm SL}$ is small. When $V_{\rm SL}$ is small, the gap is formed by a higher-order perturbation, which is probably not visible in the figure.

4.3.3 Pumped Amount and Diophantine Equation

Figure 4.8 (a) shows the pumped amount for the ground state under the condition $q_x = 3, q_y = 4, V_x = 0.5, V_y = 0.5, V_{\rm SL} = 0.25$. Since we use the plane wave approximation to calculate wave functions, there are an infinite number of bands. Only the low-lying $q_x q_y$ bands are plotted. In this case, a single band corresponds to having the $1/(q_x q_y)$ filling. The pumped amount after one cycle is -1 in the x-direction and +1 in the y-direction, which is consistent with the solution of the Diophantine equation. Also, the pumping proceeds in a staircase, which has 12 steps. This is consistent with $q_x q_y = 12$. In general, we suppose that the pumped amount which is calculated in the plane-wave approximation follows the same Diophantine equation as in the tight-binding limit. The justification of the equation is mentioned in Sec. 4.3.4.

We here focus on the fact that the band gap between the second and third excited states is large in Fig. 4.7, requiring us to treat the low-lying states below the gap carefully. Figure 4.8 (b) and (c) show the pumped amount of the first excited state and the second excited state, respectively. Also, Fig. 4.8 (d) shows the sum of (a) to (c). As mentioned earlier, the pumped amount is also represented by the Diophantine equation Eq. (126) within the plane-wave approximation. Concretely, the pumped amount when the corresponding state is located from the bottom to the r-th state is the solution of Eq. (126). Therefore, if we denote the n-th pair of Chern numbers from the bottom as (C_x, C_y) and the solution of Eq. (126) for $r = n$ as u_n, v_n, we have $C_x = u_n - u_{n-1}$, $C_y = v_n - v_{n-1}$. Table 4.2 shows the solutions of (17) for $r = 0, 1, 2, 3$ of Eq. (126) and the difference between them for $q_x = 3, q_y = 4$. The pumped amount after one period ($\phi = 2\pi$) corresponds to the difference between the adjacent solutions of the Diophantine equation, $(1, -1)$, $(-2, 3)$, and $(1, -1)$, which is listed in Table 4.2. These are consistent with Figure 8. Also, Fig. 4.8 (d) corresponds to the solution for $r = 3$ in Table 4.2.

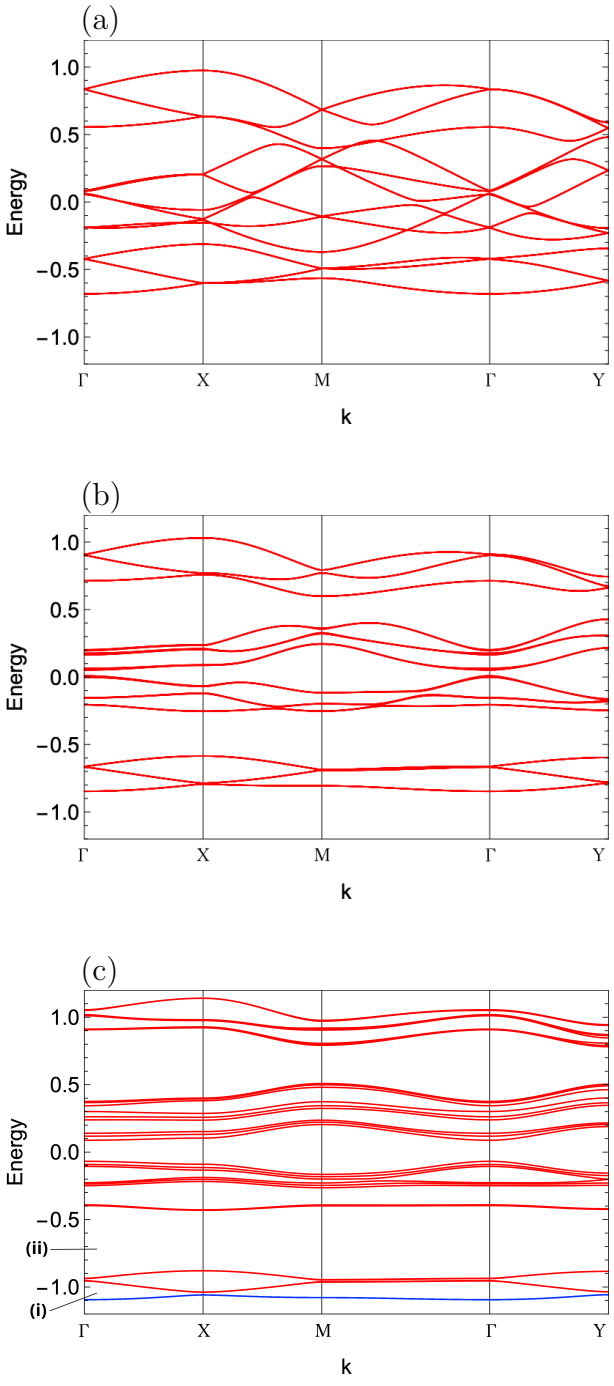

Figure 4.7: Band structure computed using the plane-wave approximation with $q_x = 3, q_y = 4, V_x = V_y = 1.0$, (a) $V_{\mathrm{SL}} = 0.1$, (b) $V_{\mathrm{SL}} = 0.3$, (c) $V_{\mathrm{SL}} = 0.5$, respectively. The blue band in (c) corresponds to the lowest band. The symbols (i) and (ii) indicate the lowest band gap and the band gap between the second and the third excited states. The high-symmetry points in the first Brillouin zone are defined as $\Gamma = (0, 0), X = (\pi, 0), Y = (0, \pi)$, and $M = (\pi, \pi)$.

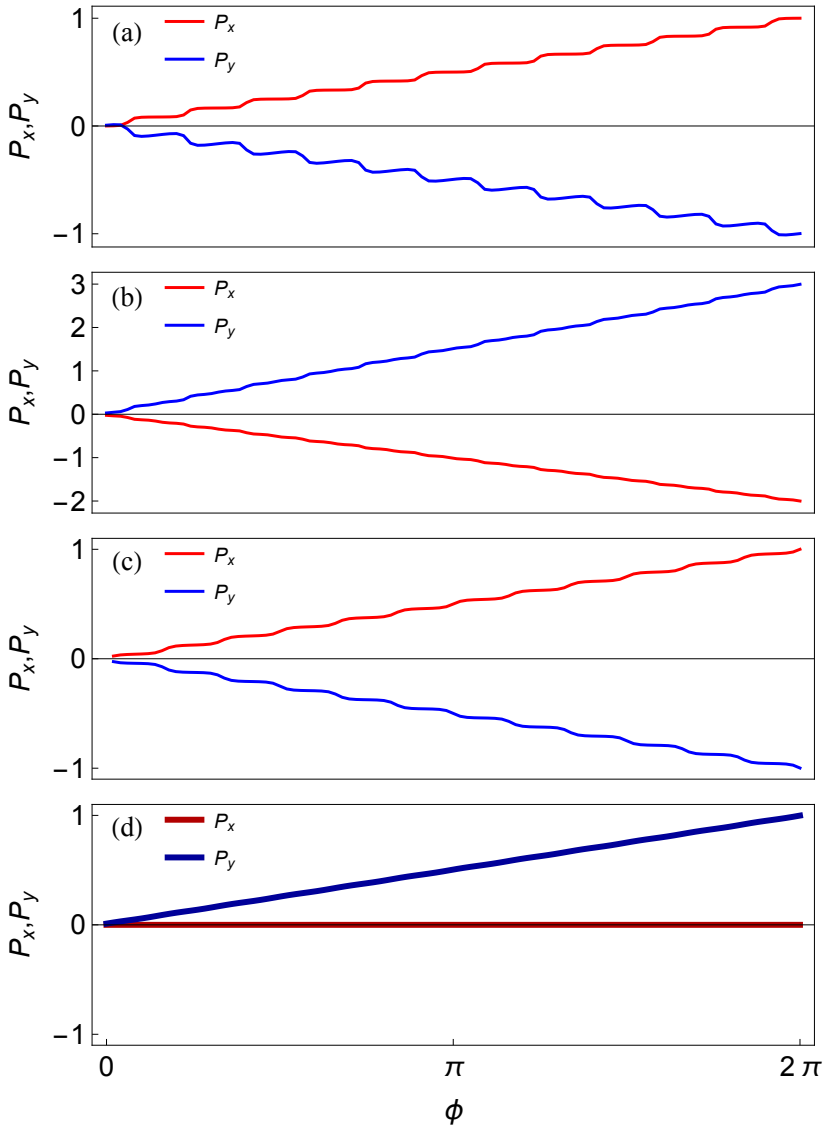

Figure 4.8: The pumped amount for the ground state, the first and the second excited state, which is calculated by integrating the Berry curvature and using the plane-wave approximation with $p_x = 3, q_x = 1, p_y = 4, q_y = 1, V_x = V_y = 2.0, V_{\mathrm{SL}} = 0.5$. The bold line in (d) shows the total of those three states. Red and blue lines correspond to x and y direction, respectively.

r	0		1		2		3
u	0	$\xrightarrow{+1}$	1	$\xrightarrow{-2}$	-1	$\xrightarrow{+1}$	0
v	0	$\xrightarrow{-1}$	-1	$\xrightarrow{+3}$	2	$\xrightarrow{-1}$	1

Table 4.2: The solutions of the Diophantine equation Eq. (145) for different r and the differences of them in the case of $q_x = 3, q_y = 4$.

We suppose that the wide band gap in $r = 3$ is generated by a first-order perturbation, while other gaps are generated by higher order perturbations. Bold lines in Fig. 4.8 (d) show the pumped amount when the states are filled up to this wide band gap. In the present case, instead of dealing only with the lowest band, we sum up the contributions of the three bands from the bottom as already mentioned. Then, the pumping in the x-direction becomes zero, and only the pumping in the y-direction remains.

We also compute the Chern numbers for various cases with different q_x and q_y. These include the case of $(q_x, q_y) = (5, 7)$ where both C_x and C_y have absolute values of 2 or larger. In every case, C_x and C_y obey the Diophantine equation Eq. (126). These results validate the claim that a pair of Chern numbers are determined by the Diophantine equation from the calculation of the Berry curvature.

4.3.4 Justification of Diophantine Equation in Plane-wave Approximation

In this section, we derive Eq. (126) from the Hamiltonian given in Eq. (146). For simplicity, let $q_x = q_y = 1$. To make the perturbation theory easier to apply, we divide the Hamiltonian in Eq. (146) into H_0 and H_1,

$$
\begin{aligned}
H &= H_0 + H_1, && (151)\\
H_0 &= \int dxdy\psi^\dagger(x,y)\Big[-\frac{\hbar^2}{2m}\frac{\partial^2}{\partial x^2} - \frac{\hbar^2}{2m}\frac{\partial^2}{\partial y^2} \\
&\quad + V_x(x,y) + V_y(x,y)\Big]\psi(x,y), && (152)\\
V_j(x,y) &= 2v_j\cos(q_j j) \quad (j = x, y), && (153)\\
H_1 &= \int dxdy\psi^\dagger(x,y)V_{\mathrm{SL}}(x,y)\psi(x,y), && (154)\\
V_{\mathrm{SL}}(x,y) &= 2v_{\mathrm{SL}}\cos(p_x x + p_y y - \varphi). && (155)
\end{aligned}
$$

First, eigenstates of H_0 can be written in Bloch states in a Brillouin zone of size $(2\pi/a, 2\pi/a)$. If H_1 is added here, some Bloch states are hybridized. This is

an idea just like the magnetic Brillouin zone. Let the Bloch state obtained from H_0 be $\hat{\psi}(k_x, k_y)$ and the corresponding eigenenergies be $E_0(k_x, k_y)$. The expression corresponding to Eq. (129) is

$$\begin{aligned} H = &- \int_{-\pi}^{\pi} \frac{dk_x}{2\pi} \int_{-\pi}^{\pi} \frac{dk_y}{2\pi} \\ &\Bigg[E_0(k_x, k_y) \hat{\psi}^\dagger(k_x, k_y, k_z) \hat{\psi}(k_x, k_y, k_z) \\ &+ \frac{V}{2} \Big(e^{-ik_z} \hat{\psi}^\dagger(k_x + 2\pi\Phi_x, k_y + 2\pi\Phi_y, k_z) \hat{\psi}(k_x, k_y, k_z) \\ &+ e^{ik_z} \hat{\psi}^\dagger(k_x - 2\pi\Phi_x, k_y - 2\pi\Phi_y, k_z) \hat{\psi}(k_x, k_y, k_z) \Big) \Bigg]. \end{aligned} \tag{156}$$

This is not diagonal because it is mixed for different (k_x, k_y). However, we can diagonalize it by using a similar method as used in Sec. 4.2.5. By expressing the single-particle states as a linear combination of different wave number states,

$$|\psi\rangle = \sum_{m=0}^{q-1} a_m \hat{\psi}^\dagger(k_x^0 + 2\pi\Phi_x m, k_y^0 + 2\pi\Phi_y m, k_z)|0\rangle, \tag{157}$$

the eigenvalue equation is obtained as follows:

$$\begin{aligned} \left(-2t\ \psi\left(k_x^0 + 2\pi\Phi_x n\right) - 2t\ \psi\left(k_y^0 + 2\pi\Phi_y n\right)\right) a_n \\ -\frac{V}{2}\left(e^{-ik_z} a_{n-1} + e^{ik_z} a_{n+1}\right) = E_{k_x^0, k_y^0, k_z} a_n. \end{aligned} \tag{158}$$

Since the eigenenergies of the Bloch state do not change so much from the cosine function, the position of the degenerate point does not change. As a result, the degree of perturbation required is determined from the degenerate point condition, which leads to the same Diophantine equation.

4.4 Effects of Harmonic Trap

So far, we have studied the continuum model Eq. (146) in the infinite system having $q_x \times q_y$-site periodicity with an integer number of filled bands. We have seen that the pumped amount is quantized and the Chern numbers obey the Diophantine equation in the infinite system. In this section, we discuss the effect of a harmonic trap on the continuum model. We consider the following Hamiltonian, where the harmonic potential as a trap is added to the continuum model Hamiltonian Eq. (146), and simulate the time evolution of the lowest energy states and their center of mass(COM).

$$H = H_{\rm cont}(x, y, t) + H_{\rm trap}(x, y) \tag{159}$$

$$H_{\rm trap} = V_{\rm trap}(x^2 + y^2) \tag{160}$$

$$i\frac{\partial}{\partial t}\Psi(t) = H\Psi(t) \tag{161}$$

For the initial state, we employ the eigenstates calculated for the initial superlattice potential. We set $\phi = 0$ when one of the lattice minima is on the minimal line of the superlattice potential. Starting from $t = 0$, we solve the time-dependent Schrödinger equation using the infinitesimal time evolution operator while the superlattice potential is changing. We set the mesh size to $\Delta x = 0.2$, and the time step to $\Delta t = 0.1$.

When the harmonic potential exists, the difference in the COM of the wave functions of the occupied states corresponds to the pumped amount. Let (x_0, y_0) be the initial COM at $t = 0$. These are not necessarily 0. We will plot the change in the COM, which is expressed as $\Delta x = x - x_0$, $\Delta y = y - y_0$. Below, we take an average of the COM of the 5 lowest energy states. Even if we change the number of states, the change in the COM does not significantly affect the pumped amount thanks to the harmonic potential, but in this case, we set the number of states to 5 to avoid edge effects. We can discuss the pumping behavior in terms of the computed COM.

In the presence of a harmonic trap, the pumping behavior turns out to be completely different between two regions. One is the weak superlattice region, in which $V_{\rm SL}$ is small compared to $V_{\rm L}$ (which is called the Hofstadter region), and the other is the strong superlattice region, in which $V_{\rm SL}$ is large (which is called the rectifying region).

4.4.1 Hofstadter Region

First, we consider the region which is near the tight-binding limit, i.e. $V_x, V_y \gg V_{\rm SL}^2/(4E_{\rm L})$. In the previous discussions, we have calculated the pumped amount by considering the integral of the Berry curvature, but this corresponds to the pumped amount when the perfectly adiabatic process is achieved. In the present case with a trap potential, we have to solve the time-dependent Schrödinger equation represented by Eq. (159). We need a new parameter of one cycle time T. In practice, the perfectly adiabatic process cannot be realized. Although the quantization of the pumped amount is lost due to the effect of the harmonic trap and the loss of the adiabaticity, the correct tendency remains for the direction and the pumped amount.

Figure 4.9 shows the COM for 5 states which have the lowest energy for varying time period T. It shows that when T is chosen so that the pumping is done at

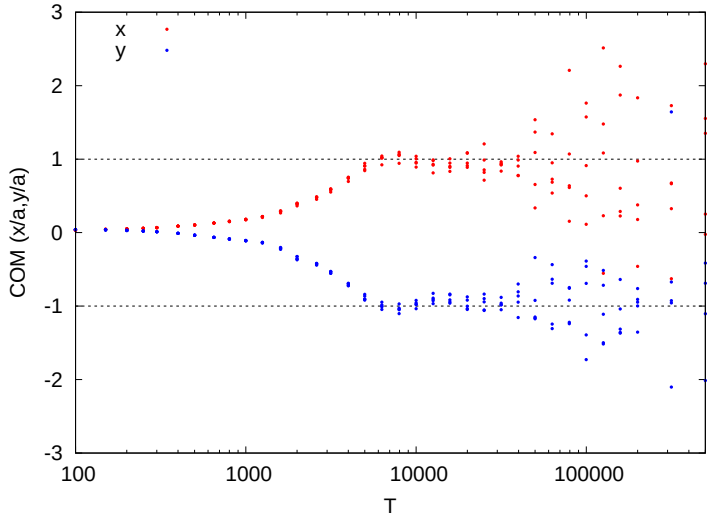

Figure 4.9: COM of each state plotted against the time period T for the lowest 5 states in the case of $q_x = 3, q_y = 4$, $V_{\text{trap}} = 0.00001$.

adequate speeds, the COM after one cycle is around $(u, v) = (1, -1)$. We can see that plateaus are found in the middle of the figure. In other words, the solutions to the Diophantine equation, discussed in the previous section, appear as the pumped amount only when T is in the range of intermediate speeds. Here we discuss why the plateaus appear in Fig. 4.9. There are three important time scales, the period of cycle T, the inverse of band-gap size $2\pi/E_{\text{gap}}$, and the inverse of the depth of harmonic trap $2\pi/E_{\text{trap}}$. When T is much smaller than $2\pi/E_{\text{gap}}$, the pumping procedure is too fast and cannot be regarded as an adiabatic process. On the other hand, when T is much larger than $2\pi/E_{\text{trap}}$, there is enough time for the COM of particles to go back to the initial position, that is, the center of the harmonic trap. As a result, T should be between $2\pi/E_{\text{gap}}$ and $2\pi/E_{\text{trap}}$ to observe clear pumping behavior. In other words, if T is too small, the particles will not be able to follow the motion of the superlattice and will be left behind, while if T is too large, because of the harmonic trap effect, the pumping does not work properly.

Figure 4.10 shows concrete examples of such pumping. Figures 4.10 (a) and (b) are the time evolution of the COM for the 5 lowest energy states in the case of (a) $q_x = 3, q_y = 4$ and (b) $q_x = 3, q_y = 5$, respectively. According to Fig. 4.10, particles are pumped in $(1, -1)$ direction for (a), and $(-1, 2)$ direction for (b). Surprisingly, while the direction of the superlattice is changed only slightly, the pumping direction is completely changed. This pumping direction can be predicted by solving Eq. (126) with the condition $r = 1$ since the lowest band contribution is dominant. For example, in the case (a), the solutions of Eq. (126) are $(u, v) = (1 + 3m, -1 + 4n)$ with integers

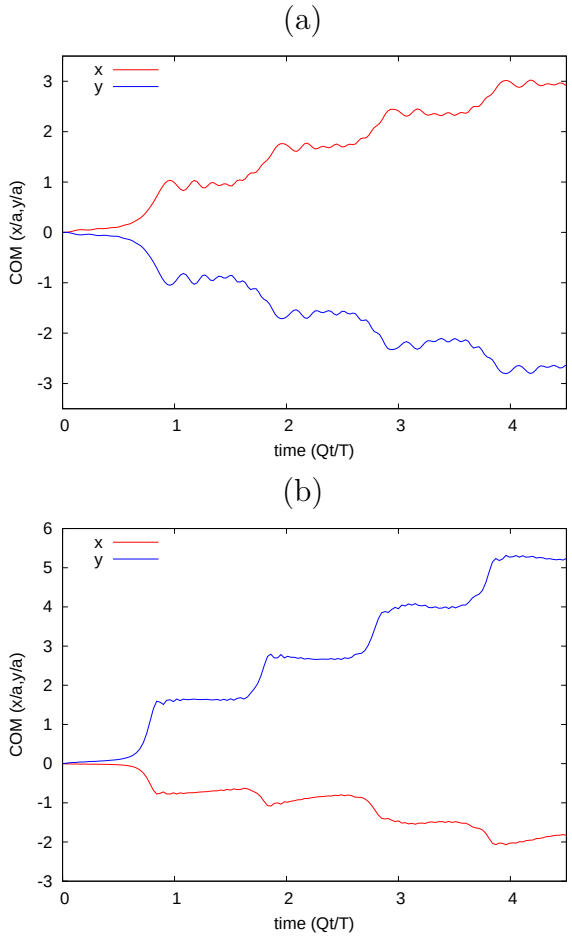

Figure 4.10: Time evolution of the average of COM for the 5 lowest energy states in the case of $V_{\mathrm{SL}} = 0.5, V_{\mathrm{trap}} = 0.00001$ and (a) $q_x = 3, q_y = 4$ and (b) $q_x = 3, q_y = 5$, respectively.

m and n. $|u|$ and $|v|$ correspond to the order of perturbation. Therefore, although there are an infinite number of solutions, only the solution where $|u|$ and $|v|$ have the smallest values is dominant. In the case (a), that is $(t_x, t_y) = (1, -1)$. Similarly, in the case (b), the solution of the Diophantine equation is $(u, v) = (-1 + 3m, 2 + 5n)$, and the dominant solution is $(u, v) = (-1, 2)$. These results are consistent with Fig. 4.10.

Observing Fig. 4.10 carefully, we find a small oscillation after the particle was pumped to the next lattice minimum. This oscillation occurs at the moment when the ground state energies in two sites become close. At that moment, the potential shape can be approximated by a double well, and the particles oscillate between the two wells. Since the angular frequency of this oscillation will be the same as

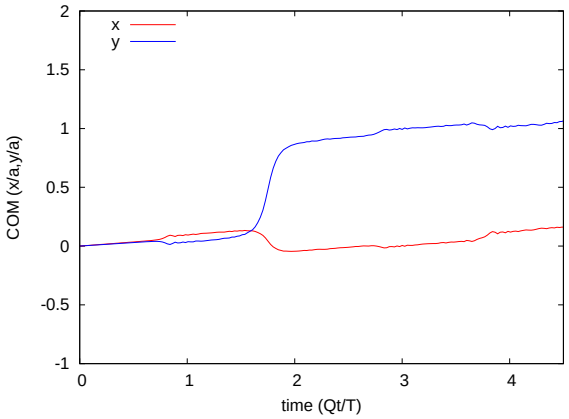

Figure 4.11: Time evolution of the average of COM for the 5 lowest energy states in the case of $V_{\mathrm{SL}} = 5.0, V_{\mathrm{trap}} = 0.00001, q_x = 3, q_y = 4$.

the hopping amplitude J, the period will be $T_{\mathrm{DW}} = 2\pi/J$. To estimate J in the optical lattice, we can use $J = \frac{4E_{\mathrm{R}}}{\sqrt{\pi}} s^{3/4} \exp(-2\sqrt{s})$ where $s = V_{\mathrm{L}}/E_{\mathrm{R}}$ and E_{R} denotes the recoil energy [120]. We have checked that this estimate is consistent with the numerical result in Fig. 4.10. We have also verified that the frequency of this small oscillation does not change while we change the time period T. This result implies that the small oscillation is caused by the pumping which is performed in finite time.

Throughout this paper, we have focused on the case $p_x = p_y = 1$, but the Diophantine equation Eq. (126) can be also applied to other cases. For the case where $p_x \neq 1$ and $p_y \neq 1$, see Sec. 4.4.3.

4.4.2 Rectifying Region

In the opposite region, where the V_{SL} term is dominant, the pumping behavior changes completely. From our numerical simulation, we find that the pumping direction is restricted to the x-axis or the y-axis exactly in this region. More precisely, the pumping direction will be whichever is closer to the x-axis or the y-axis.

When V_{SL} varies across the Hofstadter region to the rectifying region, a crossover occurs. Figures 4.10 (a), 4.11 and 4.12 provide concrete examples of such crossover. Figures 4.10 (a) and 4.11 show the time evolution of the COM for the 5 lowest energy states in the case of $q_x = 3, q_y = 4$, with (a) $V_{\mathrm{SL}} = 0.5$ and (b) $V_{\mathrm{SL}} = 5.0$, respectively. We note that only the difference of the superlattice potential depth causes the change of pumping direction. Figures 4.12 (a) and (b) show the time dependence of particle density profiles computed in the conditions corresponding to Fig. 4.10 (a) and Fig. 4.11. We can clearly see that particles move in different directions depending on whether V_{SL} is small or large.

The band structure in the previous section gives us a hint to understand why this

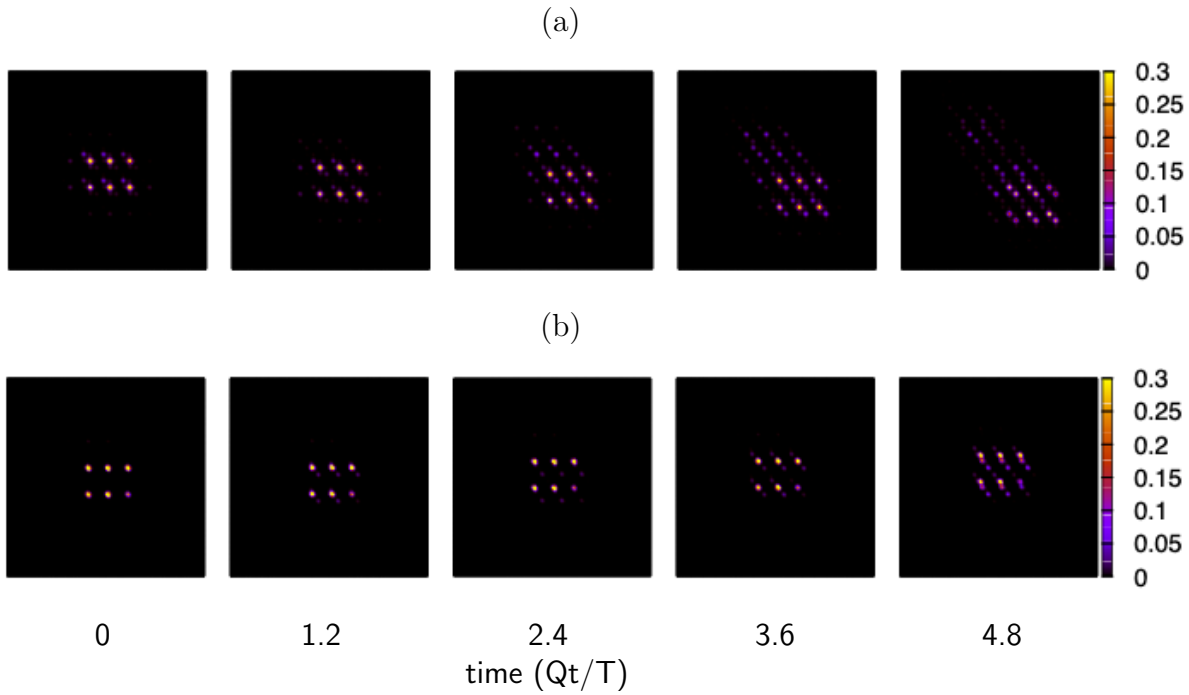

Figure 4.12: Time dependence of particle density profiles for the 5 lowest energy states in the case of $q_x = 3, q_y = 4$, with (a) $V_{\mathrm{SL}} = 0.5$ and (b) $V_{\mathrm{SL}} = 5.0$. (a) is an example of those in the Hofstadter region and (b) in the rectifying region. Horizontal and vertical axes correspond to x and y directions respectively. In (a), particles move towards positive x (right) and negative y (down) direction. On the contrary, in (b), they move towards positive y (up) direction.

crossover happens. The solution of the Diophantine equation with $r = 1$ appears when only the lowest band is considered, and pumping occurs in both the x and y-directions. On the contrary, if we compute a state which is lower than the wide band gap, pumping will occur only in the x or y-direction. The result in Fig. 4.11 suggests that the state below this wide band gap is occupied in this region. A system containing a harmonic trap has the property that a wide band gap is automatically selected without adjusting the number of particles. In the present case, by changing V_{SL}, the width of the band gap also changes, and the crossover would be caused by the change in the band gap which is automatically selected by the effect of the harmonic trap.

We note that such a change in the direction of pumping has been also studied in Ref. [101]. In Ref. [101], the topological transition in 1D systems is reported, where the Chern number of excited states is changed. On the other hand, the crossover found in our study occurs due to the effect of the harmonic trap. Since the coefficients in the

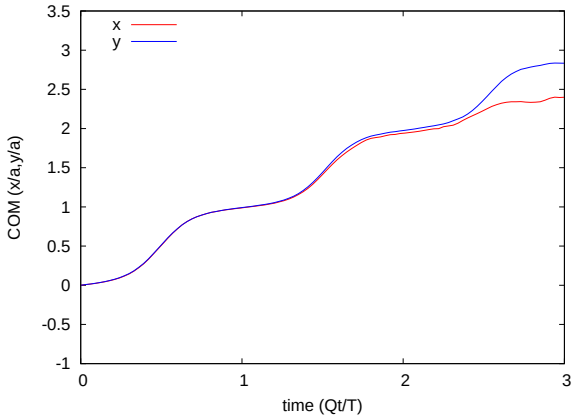

Figure 4.13: Time evolution of the average of COM for the 5 lowest energy states in the case of $V_{\mathrm{SL}} = 5.0, V_{\mathrm{trap}} = 0.00001, p_x/q_x = 2/3, p_y/q_y = 2/5$.

Bloch wave expansions of the trapped eigenstates evolve continuously as functions of V_{SL} and are not quantized due to the effect of the harmonic trap, quantization of the pumping is not complete and the topological transition does not occur.

4.4.3 Pumping in $p_x \neq 1, p_y \neq 1$ Case

Throughout this paper, we have focused on the $p_x = p_y = 1$ case. However, the obtained Diophantine equation Eq. (126) applies to other cases. Here, we show a concrete example for those cases.

Figure 4.13 shows the time evolution of the average COM in the case of $p_x/q_x = 2/3, p_y/q_y = 2/5$ where the harmonic potential exists. Since $1 \cdot 2/3 + 1 \cdot 2/5 = 16/15 = 1 + 1/15$, $(u, v) = (1, 1)$ is the solution of the Diophantine equation which corresponds to the lowest order of the perturbation. If we look at Fig. 4.13, we see that particles are pumped in the direction of the line $x = y$. We can confirm that the pumping direction and the solution of the Diophantine equation match each other in this case as well.

4.5 Summary

We have proposed a 2D version of Thouless pumping by employing a 2D square lattice tight-binding model with an obliquely introduced superlattice. We have shown that quantized particle transport occurs in this system, and the transport is expressed as a solution of the Diophantine equation. This topological nature could be understood by mapping the Hamiltonian to a 3D cubic lattice model with a homogeneous magnetic field. Moreover, we have investigated how the harmonic trap affects our model by solving the time-dependent Schrödinger equation. We have shown that plateaus appear in the plot of COM against the time period T for the superlattice sliding. When

T is in the plateau region, a nearly quantized pumping is achieved. We have found that the pumping behavior is different for two regions, which we call the Hofstadter region and the rectifying region. In the Hofstadter region, the pumped amount obeys the Diophantine equation. On the contrary, in the rectifying region, the pumping direction is restricted exactly to the x-axis or the y-axis direction. This difference causes the crossover behavior, highlighting the effect of the harmonic trap.

In summary, we have shown that the pumped amount in the 2D lattice with obliquely introduced superlattice obeys the Diophantine equation, and the harmonic trap affects the pumping behavior in various ways. The effects of the interaction and the lattice deformation are left for future studies.

Chapter 5 Conclusion

In this thesis, we have studied new topological phases which can be realized in ultracold atomic systems in optical lattice. In this chapter, we summarize this thesis.

In Chapter 1, we have introduced two hot topics: topological phases and ultracold atoms, and explained their characteristic features. The Berry phase is the phase difference which occurs when an adiabatic process whose parameter follows cyclic path in parameter space. Related to the Berry phase, the Berry connection and the Berry curvature have been defined. By integrating the Berry curvature all over the Brillouin zone, we have obtained the Chern number. The Chern number is one of the topological index which is deeply connected with topological phases. The transport properties of Integer quantum Hall effect system and Thouless pumping system are described by Chern number. Also, there exists a mapping between these two systems, and they are mathematically equivalent. Ultracold atoms are atoms that are trapped in vacuum by using magnetic or optical field, and maintained at temperatures usually below microkelvin (μK) order. There are three outstanding properties in these systems, 1. High controllability of physical parameters, 2. Richness of detection methods, 3. Exotic phases realization by using synthetic gauge field. Numerous kinds of topological phases are realized in ultracold atoms system.

In Chapter 2, we have presented the numerical methods which we have used in this thesis, exact diagonalization and DMRG. Exact diagonalization is a numerical computation method which calculates the eigenenergies and the eigenstate by writing up all of the bases of the system and diagonalizing the Hamiltonian matrix. We have used Lanczos method, which is good when the Hamiltonian is sparse and the dimension of Hilbert space is up to about $\sim 10^8$. When the dimension of Hilbert space is much larger than $\sim 10^8$, it is hard to use exact diagonalization, but if the system is 1D, Density matrix renormalization group (DMRG) is one of the most effective method. In DMRG, we separate the whole system into a system and an environment, and we enlarge the system and environment one site by one site. While enlarging the system, we choose eigenvalues/eigenvectors which we should left. To choose them, we take a partial trace for environment and leave the eigenvectors which have larger eigenvalues of its density matrix. This method succeeded in many 1D models. Also, we have introduced Fukui-Hatsugai-Suzuki method, which enables us to calculate a Chern number by calculating only for discretized points of the Brillouin zone without

worrying about gauge choice. Finally, we have presented an effective method to calculate time-dependent Schrödinger equation.

In Chapter 3, we have studied a quasiperiodic Bose-Hubbard model with interaction by using exact diagonalization and DMRG. We have shown that the energy gap of the Harper-type Bose-Hubbard model increases as the on-site interaction strength U increases when $U > U_c$ ($\sim 0.25t$), and at the same time, topological number (Chern number) stays non-zero and constant. Also, there are two typical quasiperiodic models, the Harper model and the Fibonacci model. The topological equivalence between these models is known. We have introduced the on-site interaction to these models, and have shown that the topological equivalence also exists between interacting quasiperiodic systems, the Harper-type and Fibonacci-type Bose-Hubbard models. Furthermore, we have investigated the phase diagram, which includes superfluid, Bose glass, and incommensurate charge density wave, as a function of the potential deformation parameter β and the interaction strength U.

In Chapter 4, we have considered a 2D version of Thouless pumping by employing a 2D square lattice tight-binding model with an obliquely introduced potential. We have studied three models, the tight-binding model, the continuum model, and the model with harmonic trap potential. The topological nature of the tight-binding model with obliquely introduced superlattice can be understood by mapping the 2D Hamiltonian to a 3D cubic lattice model with a homogeneous magnetic field. Also, we have shown that quantized particle transport occurs in both the tight-binding model and the continuum model, and the transport is expressed as a solution of the Diophantine equation. Moreover, we have studied the effect of the harmonic trap by solving the time-dependent Schrödinger equation. Under the harmonic trap, we have found that the pumping behavior is different for two regions, which we call the Hofstadter region and the rectifying region. In the Hofstadter region, we have shown that a nearly quantized pumping occurs when the phase of the superlattice potential is changed at an appropriate speed. This quantized pumping obeys the Diophantine equation. On the contrary, in the rectifying region, the pumping direction is restricted exactly to the x-axis or the y-axis direction. We have found that the harmonic trap causes the crossover between two regions, the Hofstadter region and the rectifying region.

In this thesis, we have considered a 1D system with the interaction in Chapter 3 and considered a 2D noninteracting system in Chapter 4. Therefore, a 2D system with interaction, which is more practical for an experimental setup, is left for a future problem.

Bibliography

[1] M. V. Berry, Proc. R. Soc. London. A. **392**, 45 (1984).

[2] D. J. Thouless, Phys. Rev. B **27**, 6083 (1983).

[3] K. V. Klitzing, G. Dorda, and M. Pepper, Phys. Rev. Lett. **45**, 494 (1980).

[4] D. J. Thouless, M. Kohmoto, M. P. Nightingale, and M. den Nijs, Phys. Rev. Lett. **49**, 405 (1982).

[5] D. R. Hofstadter, Phys. Rev. B **14**, 2239 (1976).

[6] R. P. Feynman, Int. J. Theor. Phys. **21**, 467 (1982).

[7] A. J. Moerdijk, B. J. Verhaar, and A. Axelsson, Phys. Rev. A **51**, 4852 (1995).

[8] C. Chin, R. Grimm, P. Julienne, and E. Tiesinga, Rev. Mod. Phys. **82**, 1225 (2010).

[9] P. B. Blakie and C. W. Clark, J. Phys. B **37**, 1391 (2004).

[10] C. Becker, P. Soltan-Panahi, J. Kronjäger, S. Dörscher, K. Bongs, and K. Sengstock, New J. Phys. **12**, 065025 (2010).

[11] M. P. A. Fisher, P. B. Weichman, G. Grinstein, and D. S. Fisher, Phys. Rev. B **40**, 546 (1989).

[12] D. Jaksch, C. Bruder, J. I. Cirac, C. W. Gardiner, and P. Zoller, Phys. Rev. Lett. **81**, 3108 (1998).

[13] M. Greiner, O. Mandel, T. Esslinger, T. W. Hänsch, and I. Bloch, Nature **415**, 39 (2002).

[14] R. Jördens, N. Strohmaier, K. Günter, H. Moritz, and T. Esslinger, Nature **455**, 204 (2008).

[15] U. Schneider, L. Hackermüller, S. Will, T. Best, I. Bloch, T. A. Costi, R. W. Helmes, D. Rasch, and A. Rosch, Science **322**, 1520 (2008).

[16] S. Taie, R. Yamazaki, S. Sugawa, and Y. Takahashi, Nat. Phys. **8**, 825 (2012).

[17] C. Hofrichter, L. Riegger, F. Scazza, M. Höfer, D. R. Fernandes, I. Bloch, and S. Fölling, Phys. Rev. X **6**, 021030 (2016).

[18] T. M. Brzozowski, M. Maczynska, M. Zawada, J. Zachorowski, and W. Gawlik, J. Opt. B **4**, 62 (2002).

[19] E. Altman, E. Demler, and M. D. Lukin, Phys. Rev. A **70**, 013603 (2004).

[20] B. Fang, A. Johnson, T. Roscilde, and I. Bouchoule, Phys. Rev. Lett. **116**, 050402 (2016).

[21] J. F. Sherson, C. Weitenberg, M. Endres, M. Cheneau, I. Bloch, and S. Kuhr, Nature **467**, 68 (2010).

[22] K. W. Madison, F. Chevy, W. Wohlleben, and J. Dalibard, Phys. Rev. Lett. **84**, 806 (2000).

[23] J. R. Abo-Shaeer, C. Raman, J. M. Vogels, and W. Ketterle, Science **292**, 476 (2001).

[24] P. Engels, I. Coddington, P. C. Haljan, V. Schweikhard, and E. A. Cornell, Phys. Rev. Lett. **90**, 170405 (2003).

[25] S. Nakajima, T. Tomita, S. Taie, T. Ichinose, H. Ozawa, L. Wang, M. Troyer, and Y. Takahashi, Nat. Phys. **12**, 296 (2016).

[26] Y. Ke, X. Qin, Y. S. Kivshar, and C. Lee, Phys. Rev. A **95**, 063630 (2017).

[27] M. Atala, M. Aidelsburger, J. T. Barreiro, D. Abanin, T. Kitagawa, E. Demler, and I. Bloch, Nat. Phys. **9**, 795 (2013).

[28] G. Jotzu, M. Messer, R. Desbuquois, M. Lebrat, T. Uehlinger, D. Greif, and T. Esslinger, Nature **515**, 237 (2014).

[29] M. Schreiber, S. S. Hodgman, P. Bordia, H. P. Lüschen, M. H. Fischer, R. Vosk, E. Altman, U. Schneider, and I. Bloch, Science **349**, 842 (2015).

[30] N. Goldman, I. Satija, P. Nikolic, A. Bermudez, M. A. Martin-Delgado, M. Lewenstein, and I. B. Spielman, Phys. Rev. Lett. **105**, 255302 (2010).

[31] L. Mazza, A. Bermudez, N. Goldman, M. Rizzi, M. A. Martin-Delgado, and M. Lewenstein, New J. Phys. **14**, 015007 (2012).

[32] D.-W. Zhang, S.-L. Zhu, and Z. D. Wang, Phys. Rev. A **92**, 013632 (2015).

[33] B. Béri and N. R. Cooper, Phys. Rev. Lett. **107**, 145301 (2011).

[34] D.-L. Deng, S.-T. Wang, K. Sun, and L.-M. Duan, Chin. Phys. Lett. **35**, 013701 (2017).

[35] A. Celi, P. Massignan, J. Ruseckas, N. Goldman, I. B. Spielman, G. Juzeliūnas, and M. Lewenstein, Phys. Rev. Lett. **112**, 043001 (2014).

[36] M. Mancini, G. Pagano, G. Cappellini, L. Livi, M. Rider, J. Catani, C. Sias, P. Zoller, M. Inguscio, M. Dalmonte, and L. Fallani, **349**, 1510 (2015).

[37] B. K. Stuhl, H.-I. Lu, L. M. Aycock, D. Genkina, and I. B. Spielman, **349**, 1514 (2015).

[38] H. M. Price, O. Zilberberg, T. Ozawa, I. Carusotto, and N. Goldman, Phys. Rev. Lett. **115**, 195303 (2015).

[39] C. Lanczos, J. Res. Natl. Bur. Stand. B **45**, 255 (1950).

[40] S. R. White, Phys. Rev. Lett. **69**, 2863 (1992).

[41] S. R. White, Phys. Rev. B **48**, 10345 (1993).

[42] F. Verstraete and J. I. Cirac, (2004), arXiv:cond-mat/0407066 .

[43] U. Schollwöck, Annals of Physics **326**, 96 (2011), january 2011 Special Issue.

[44] T. Fukui, Y. Hatsugai, and H. Suzuki, J. Phys. Soc. Jpn. **74**, 1674 (2005).

[45] N. Watanabe, URL: http://cms.phys.s.u-tokyo.ac.jp/∼naoki/ .

[46] D. Shechtman, I. Blech, D. Gratias, and J. W. Cahn, Phys. Rev. Lett. **53**, 1951 (1984).

[47] T. Fujiwara and Y. Ishii, *Quasicrystals*, edited by T. Fujiwara and Y. Ishii, Handbook of Metal Physics, Vol. 3 (Elsevier, 2008) pp. 1 – 9.

[48] L. Bindi, P. J. Steinhardt, N. Yao, and P. J. Lu, Science **324**, 1306 (2009).

[49] S. Förster, K. Meinel, R. Hammer, M. Trautmann, and W. Widdra, Nature **502**, 215 (2013).

[50] N. A. Wasio, R. C. Quardokus, R. P. Forrest, C. S. Lent, S. A. Corcelli, J. A. Christie, K. W. Henderson, and S. A. Kandel, Nature **507**, 86 (2014).

[51] M. Z. Hasan and C. L. Kane, Rev. Mod. Phys. **82**, 3045 (2010).

[52] X.-L. Qi and S.-C. Zhang, Rev. Mod. Phys. **83**, 1057 (2011).

[53] L.-J. Lang, X. Cai, and S. Chen, Phys. Rev. Lett. **108**, 220401 (2012).

[54] Y. E. Kraus, Y. Lahini, Z. Ringel, M. Verbin, and O. Zilberberg, Phys. Rev. Lett. **109**, 106402 (2012).

[55] I. I. Satija and G. G. Naumis, Phys. Rev. B **88**, 054204 (2013).

[56] K. A. Madsen, E. J. Bergholtz, and P. W. Brouwer, Phys. Rev. B **88**, 125118 (2013).

[57] Y. E. Kraus, Z. Ringel, and O. Zilberberg, Phys. Rev. Lett. **111**, 226401 (2013).

[58] Y. E. Kraus and O. Zilberberg, Phys. Rev. Lett. **109**, 116404 (2012).

[59] P. G. Harper, Proc. Phys. Soc. A **68**, 874 (1955).

[60] M. Y. Azbel, Phys. Rev. Lett. **43**, 1954 (1979).

[61] S. Aubry and G. André, Proceedings, VIII International Colloquium on Group-Theoretical Methods in Physics **3** (1980).

[62] L. Fallani, J. E. Lye, V. Guarrera, C. Fort, and M. Inguscio, Phys. Rev. Lett. **98**, 130404 (2007).

[63] V. I. Yukalov, Laser Phys. **19**, 1 (2009).

[64] L. Tanzi, E. Lucioni, S. Chaudhuri, L. Gori, A. Kumar, C. D'Errico, M. Inguscio, and G. Modugno, Phys. Rev. Lett. **111**, 115301 (2013).

[65] J. Vidal, D. Mouhanna, and T. Giamarchi, Phys. Rev. Lett. **83**, 3908 (1999).

[66] G. Roux, T. Barthel, I. P. McCulloch, C. Kollath, U. Schollwöck, and T. Giamarchi, Phys. Rev. A **78**, 023628 (2008).

[67] S. K. Adhikari and L. Salasnich, Phys. Rev. A **80**, 023606 (2009).

[68] F. Schmitt, M. Hild, and R. Roth, Phys. Rev. A **80**, 023621 (2009).

[69] G. Orso, A. Iucci, M. A. Cazalilla, and T. Giamarchi, Phys. Rev. A **80**, 033625 (2009).

[70] M. Albert and P. Leboeuf, Phys. Rev. A **81**, 013614 (2010).

[71] Y. Cheng and S. K. Adhikari, Phys. Rev. A **81**, 023620 (2010).

[72] X. Cai, S. Chen, and Y. Wang, Phys. Rev. A **81**, 023626 (2010).

[73] A. Cetoli and E. Lundh, Phys. Rev. A **81**, 063635 (2010).

[74] T. Roscilde, Phys. Rev. A **82**, 023601 (2010).

[75] M. Tezuka and A. M. García-García, Phys. Rev. A **82**, 043613 (2010).

[76] A. Dhar, T. Mishra, R. V. Pai, and B. P. Das, Phys. Rev. A **83**, 053621 (2011).

[77] G. Dufour and G. Orso, Phys. Rev. Lett. **109**, 155306 (2012).

[78] X. Cai, L.-J. Lang, S. Chen, and Y. Wang, Phys. Rev. Lett. **110**, 176403 (2013).

[79] P. Ribeiro, M. Haque, and A. Lazarides, Phys. Rev. A **87**, 043635 (2013).

[80] S.-L. Zhu, Z. D. Wang, Y. H. Chan, and L. M. Duan, Phys. Rev. Lett. **110**, 075303 (2013).

[81] X. Deng and L. Santos, Phys. Rev. A **89**, 033632 (2014).

[82] L. Wang, M. Troyer, and X. Dai, Phys. Rev. Lett. **111**, 026802 (2013).

[83] F. Grusdt, M. Höning, and M. Fleischhauer, Phys. Rev. Lett. **110**, 260405 (2013).

[84] R. B. Laughlin, Phys. Rev. B **23**, 5632 (1981).

[85] B. I. Halperin, Phys. Rev. B **25**, 2185 (1982).

[86] Y. Hatsugai, Phys. Rev. Lett. **71**, 3697 (1993).

[87] J. E. Avron, R. Seiler, and B. Simon, Phys. Rev. Lett. **51**, 51 (1983).

[88] Q. Niu, D. J. Thouless, and Y.-S. Wu, Phys. Rev. B **31**, 3372 (1985).

[89] M. Kohmoto, Ann. Phys. **160**, 343 (1985).

[90] G. Montambaux and M. Kohmoto, Phys. Rev. B **41**, 11417 (1990).

[91] M. Kohmoto, B. I. Halperin, and Y.-S. Wu, Phys. Rev. B **45**, 13488 (1992).

[92] M. Koshino, H. Aoki, K. Kuroki, S. Kagoshima, and T. Osada, Phys. Rev. Lett. **86**, 1062 (2001).

[93] M. Koshino, H. Aoki, T. Osada, K. Kuroki, and S. Kagoshima, Phys. Rev. B **65**, 045310 (2002).

[94] R. O. Umucal ılar and I. Carusotto, Phys. Rev. A **84**, 043804 (2011).

[95] M. Hafezi, E. A. Demler, M. D. Lukin, and J. M. Taylor, Nat. Phys. **7**, 907 (2011).

[96] A. B. Khanikaev, S. Hossein Mousavi, W.-K. Tse, M. Kargarian, A. H. MacDonald, and G. Shvets, Nat. Mater. **12**, 233 (2013).

[97] J. Dalibard, F. Gerbier, G. Juzeliunas, and P. Öhberg, Rev. Mod. Phys. **83**, 1523 (2011).

[98] M. Aidelsburger, M. Atala, M. Lohse, J. T. Barreiro, B. Paredes, and I. Bloch, Phys. Rev. Lett. **111**, 185301 (2013).

[99] H. Miyake, G. A. Siviloglou, C. J. Kennedy, W. C. Burton, and W. Ketterle, Phys. Rev. Lett. **111**, 185302 (2013).

[100] Q. Niu, Phys. Rev. B **34**, 5093 (1986).

[101] M. Lohse, C. Schweizer, O. Zilberberg, M. Aidelsburger, and I. Bloch, Nat. Phys. **12**, 350 (2015).

[102] J.-T. A. Chiang and Q. Niu, Phys. Rev. A **57**, R2278 (1998).

[103] O. Romero-Isart and J. J. García-Ripoll, Phys. Rev. A **76**, 052304 (2007).

[104] Y. Qian, M. Gong, and C. Zhang, Phys. Rev. A **84**, 013608 (2011).

[105] F. Mei, J.-B. You, D.-W. Zhang, X. C. Yang, R. Fazio, S.-L. Zhu, and L. C. Kwek, Phys. Rev. A **90**, 063638 (2014).

[106] D.-W. Zhang, F. Mei, Z.-Y. Xue, S.-L. Zhu, and Z. D. Wang, Phys. Rev. A **92**, 013612 (2015).

[107] R. Wei and E. J. Mueller, Phys. Rev. A **92**, 013609 (2015).

[108] P. Marra and R. Citro, The European Physical Journal Special Topics **226**, 2781 (2017).

[109] Y.-B. Yang, L.-M. Duan, and Y. Xu, Phys. Rev. B **98**, 165128 (2018).

[110] P. Marra and M. Nitta, (2020), arXiv:2001.11022 .

[111] M. Nakagawa, T. Yoshida, R. Peters, and N. Kawakami, Phys. Rev. B **98**, 115147 (2018).

[112] L. Taddia, E. Cornfeld, D. Rossini, L. Mazza, E. Sela, and R. Fazio, Phys. Rev. Lett. **118**, 230402 (2017).

[113] A. Hayward, C. Schweizer, M. Lohse, M. Aidelsburger, and F. Heidrich-Meisner, Phys. Rev. B **98**, 245148 (2018).

[114] L. Privitera, A. Russomanno, R. Citro, and G. E. Santoro, Phys. Rev. Lett. **120**, 106601 (2018).

[115] S. Hu, Y. Ke, Y. Deng, and C. Lee, Phys. Rev. B **100**, 064302 (2019).

[116] S. Greschner, S. Mondal, and T. Mishra, Phys. Rev. A **101**, 053630 (2020).

[117] L. Arceci, L. Kohn, A. Russomanno, and G. E. Santoro, J. Stat. Mech.: Theory Exp. **2020**, 043101 (2020).

[118] M. Lohse, C. Schweizer, H. M. Price, O. Zilberberg, and I. Bloch, Nature **553**, 55 (2018).

[119] P. B. Blakie and J. V. Porto, Phys. Rev. A **69**, 013603 (2004).

[120] I. Bloch, J. Dalibard, and W. Zwerger, Rev. Mod. Phys. **80**, 885 (2008).

[121] J. Yang and Z. H. Musslimani, Opt. Lett. **28**, 2094 (2003).

[122] P. Soltan-Panahi, J. Struck, P. Hauke, A. Bick, W. Plenkers, G. Meineke, C. Becker, P. Windpassinger, M. Lewenstein, and K. Sengstock, Nat. Phys. **7**, 434 (2011).

[123] S. Taie, H. Ozawa, T. Ichinose, T. Nishio, S. Nakajima, and Y. Takahashi, Sci. Adv. **1**, 1500854 (2015).

[124] R. O. Umucalılar, H. Zhai, and M. O. Oktel, Phys. Rev. Lett. **100**, 070402 (2008).

[125] T. D. Stanescu, V. Galitski, J. Y. Vaishnav, C. W. Clark, and S. Das Sarma, Phys. Rev. A **79**, 053639 (2009).

[126] Z. Lan, N. Goldman, A. Bermudez, W. Lu, and P. Öhberg, Phys. Rev. B **84**, 165115 (2011).

[127] B. Liu and L. Yin, Phys. Rev. A **86**, 031603 (2012).

[128] T. D. Stanescu, V. Galitski, and S. Das Sarma, Phys. Rev. A **82**, 013608 (2010).

[129] D.-W. Zhang, Y. X. Zhao, R.-B. Liu, Z.-Y. Xue, S.-L. Zhu, and Z. D. Wang, Phys. Rev. A **93**, 043617 (2016).

[130] N. Goldman, G. Jotzu, M. Messer, F. Görg, R. Desbuquois, and T. Esslinger, Phys. Rev. A **94**, 043611 (2016).

[131] L. Jin, Phys. Rev. A **96**, 032103 (2017).

[132] H. Kim, G. Zhu, J. V. Porto, and M. Hafezi, Phys. Rev. Lett. **121**, 133002 (2018).

[133] N. Goldman, J. Dalibard, A. Dauphin, F. Gerbier, M. Lewenstein, P. Zoller, and I. B. Spielman, Proc. Nat. Acad. Sci. **110**, 6736 (2013).

[134] X. Li, E. Zhao, and W. Vincent Liu, Nat. Commun. **4**, 1523 (2013).

[135] X.-T. Xu, Z.-Y. Wang, R.-H. Jiao, C.-R. Yi, W. Sun, and S. Chen, Rev. Sci. Instrum. **90**, 054708 (2019).

[136] B. Song, C. He, S. Niu, L. Zhang, Z. Ren, X.-J. Liu, and G.-B. Jo, Nat. Phys. **15**, 911 (2019).

[137] S. de Léséleuc, V. Lienhard, P. Scholl, D. Barredo, S. Weber, N. Lang, H. P. Büchler, T. Lahaye, and A. Browaeys, Science **365**, 775 (2019).

[138] N. R. Cooper, J. Dalibard, and I. B. Spielman, Rev. Mod. Phys. **91**, 015005 (2019).

[139] C. Schweizer, M. Lohse, R. Citro, and I. Bloch, Phys. Rev. Lett. **117**, 170405 (2016).

[140] Y. Cao, V. Fatemi, S. Fang, K. Watanabe, T. Taniguchi, E. Kaxiras, and P. Jarillo-Herrero, Nature **556**, 43 (2018).

[141] J. M. B. Lopes dos Santos, N. M. R. Peres, and A. H. Castro Neto, Phys. Rev. Lett. **99**, 256802 (2007).

[142] A. Rozhkov, A. Sboychakov, A. Rakhmanov, and F. Nori, Phys. Rep. **648**, 1 (2016).

[143] E. Suárez Morell, J. D. Correa, P. Vargas, M. Pacheco, and Z. Barticevic, Phys. Rev. B **82**, 121407 (2010).

[144] R. de Gail, M. O. Goerbig, F. Guinea, G. Montambaux, and A. H. Castro Neto, Phys. Rev. B **84**, 045436 (2011).

[145] R. Bistritzer and A. H. MacDonald, Phys. Rev. B **84**, 035440 (2011).

[146] R. Resta and D. Vanderbilt, *Theory of Polarization: A Modern Approach*, Vol. 105 (2007) pp. 31–68.

Acknowledgment

First of all, I would like to express my sincerest gratitude to Prof. Norio Kawakami for his kind and warmhearted support, encouragement, and productive discussions during my graduate course. His great insight and deep knowledge of condensed matter physics always helped me to progress our research. He taught me not only physics, but many other things as well. Without his persistent help, this thesis could not have been completed.

I am also deeply grateful to Prof. Masaki Tezuka for the collaboration and fruitful discussions. His continuing support helped me and encouraged me a lot. I have learned how to perform numerical calculation from him. I would like to express my deep appreciation to him for taking his time to give me numerous words of advice.

I would like to thank Prof. Manfred Sigrist for his support and kindness during my visit to ETH Zürich. It was stimulating to discuss about condensed matter physics with him. I would like to express my gratitude to current and former staff members in the Condensed Matter Theory Group, Prof. Youichi Yanase, Prof. Ryusuke Ikeda, Prof. Robert Peters, for their advices and comments in various opportunities. Also, I would like to thank my colleagues, Mr. Tomohiro Hisamitsu, Dr. Kenichi Hosoya, Mr. Yohei Ibe, Mr. Koudai Iwahori, Mr. Yoshihiro Michishita, Mr. Yu Ogata, Dr. Atsuo Shitade, Dr. Kazuaki Takasan, and Mr. Kazuki Yamamoto.

I would like to thank my friends, Dr. Takahiro Doi, Mr. Kenta Moriyama, Dr. Masaya Nakagawa, Dr. Yasuharu Nakamura, Dr. Takuya Nomoto, Dr. Tokiro Numasawa, Dr. Hiroaki Sumiyoshi, and Dr. Shoichiro Tsutsui for enjoyable conversations in my daily life. It was a great pleasure for me to study physics with them.

I would like to acknowledge the financial support from Japan Society for the Promotion of Science (JSPS) KAKENHI (Grant No. JP15J02158) and JSPS Research Fellowship for Young Scientists.

Last but not least, I would like to express my deepest gratitude to my family, Mitsuo Matsuda, Yumiko Matsuda, Asahiko Matsuda, and Sachiko Matsuda, for continuous encouragement and financial support.